

Ultrasound-induced modulation of longitudinal relaxation rates in superparamagnetic iron oxide nanoparticle solutions

by

Kaj Polman

in partial fulfilment of the requirements of Master of Science in Biomedical Engineering,
Track Medical Physics,
at the Delft University of Technology,
to be defended publicly on Tuesday July 8, 2025 at 10:30.

Student number: 4966015

Project duration: Nov 11, 2024 - Jul 8, 2025

Thesis committee: Dr. S.D. Weingärtner (chair), TU Delft, main supervisor

Dr. M. Božić-Iven, TU Delft, daily supervisor

Dr.ir. M.D. Verweij, TU Delft Dr. H.J. Geertsema, TU Delft

An electronic version of this thesis is available at https://repository.tudelft.nl/



Acknowledgements

I would like to express my gratitude to several individuals for their assistance during the completion of my thesis.

First of all, I would like to thank Maša Božić-Iven for the daily supervision and consistent support. Her feedback and willingness to help have helped me tremendously in the progress of my work.

Secondly, I am also very grateful to Sebastian Weingärtner for the many insightful and stimulating discussions that helped deepen my understanding of the subject.

Finally, I would like to give a special thanks to the committee members for their time and evaluation of my work.

Kaj Polman Delft, July 2025

Abstract

This thesis investigates the combination of Nuclear Magnetic Resonance (NMR) and Ultrasound (US), referred to as Acoustic NMR (ANMR), to modulate longitudinal relaxation rates (R_1) in aqueous solutions of superparamagnetic iron oxide nanoparticles (SPIONs). By enabling the modulation of relaxation rates, ANMR could serve as a promising technique for low-field MRI. The aim of this work is twofold. Firstly, a theoretical model is developed to describe the dynamics of SPION clusters under the influence of US waves to estimate the effect of rotational and translational motion on the fluctuation in the local magnetic field. Secondly, experimental ANMR measurements are conducted on three aqueous SPION suspensions with particle diameters of 50, 130, and 300 nm to investigate the effect of particle size on the longitudinal relaxation rate.

The model predicts that translational motion of SPION aggregates contributes more significantly to the longitudinal relaxation rate than rotational motion. The modeled spectral density confirms a distinct peak at the US driving frequency, suggesting that the SPION clusters exhibit resonant magnetic field fluctuations with the Larmor frequency. Experimental ANMR results show no significant change in the longitudinal relaxation rate for all three SPION solutions, indicating that the delivered acoustic pressure is potentially insufficient. By overcoming current experimental limitations, ANMR holds great promise as a novel contrast mechanism for low-field MRI, potentially enabling localized contrast enhancements.

Contents

Ac	knov	wledgements	ii		
Ak	stra	ct	iν		
No	men	clature	/iii		
1	Introduction 1				
2	2.1 2.2 2.3 2.4 2.5	Nuclear Magnetic Resonance 2.1.1 Nuclear Magnetism 2.1.2 Principles of NMR 2.1.3 Relaxation and Bloch equations 2.1.4 Relaxation mechanisms SPIONs Ultrasound and particle dynamics 2.3.1 Basics of US 2.3.2 Particle dynamics The principles of Acoustic NMR	3 3 4 5 6 7 8 8 10 11		
3	Met l 3.1 3.2 3.3	Ultrasound-modulated SPION relaxation model $3.1.1$ Equations of motion $3.1.2$ Cluster size $3.1.3$ k-Wave toolbox $3.1.4$ Local magnetic field fluctuations $3.1.5$ Autocorrelation function $3.1.6$ Determination of R_1 Preparatory NMR measurements $3.2.1$ Measuring T_1 $3.2.2$ Measuring T_2 Acoustic NMR measurements $3.3.1$ SPION solutions $3.3.2$ ANMR sequence	13 14 15 16 17 17 18 19 19 19		
4	Res 4.1	Ultrasound-modulated SPION relaxation model	22 22 22 25 27		
5	5.1	Ultrasound-modulated SPION relaxation model	29 29 29 30 30		
6	Con	nclusion	32		
R	foro	PACE	33		

V11
VII

Α	Acoustic radiation force in standing wave	38
В	Determining factors for SPION aggregation B.1 Brownian motion	41
С	Preparatory T_1 and T_2 NMR measurements	43
D	T_1 and T_2 NMR measurements over time	45

Nomenclature

Abbreviations

Abbreviation	Definition
NMR	Nuclear Magnetic Resonance
ANMR	Acoustic Nuclear Magnetic Resonance
MRI	Magnetic Resonance Imaging
US	Ultrasound
RF	Radio frequency
T_1	Longitudinal relaxation time
R_1	Longitudinal relaxation rate
T_2	Transverse relaxation time
R_2	Transverse relaxation rate
FID	Free Induction Decay
BPP theory	Bloembergen-Purcell-Pound theory
SPIONs	Superparamagnetic iron oxide nanoparticles
DLCA	Diffusion-limited cluster aggregation
FFT	Fast Fourier Transform
SR	Saturation recovery
CPMG	Carr-Purcell-Meiboom-Gill
AFG	Arbitrary function generator
D	Dextran
CLD	Cross-linked dextran
PEG	Polyethylene glycol
NMRD	Nuclear Magnetic Relaxation Dispersion

Introduction

Nuclear Magnetic Resonance (NMR), first described by Rabi in 1938 [1], is a quantum mechanical phenomenon in which an ensemble of atomic nuclei interacts with an external magnetic field. This results in the formation of a net magnetization, which can be detected and used to create an image in Magnetic Resonance Imaging (MRI). When exposed to a weaker radio frequency (RF) pulse, the nuclei absorb energy and are excited to higher energy states. After the RF pulse, the nuclei undergo a process called relaxation, where the net magnetization of the sample returns to equilibrium. As relaxation processes strongly depend on the interaction strength between nuclei and their surroundings, various biological tissues exhibit different relaxation rates. This variation contributes to the rich soft-tissue contrast that makes MRI a powerful and widely used diagnostic tool in clinical practice.

Ultrasound (US) is based on a very different physical phenomenon from MRI, which uses sound waves of a frequency above the human hearing range. In US imaging, the scattered echoes are detected to generate the image and give information about the type of tissue and its location. One of the few similarities between MRI and US imaging is that both techniques are non-invasive and are operable in similar frequency ranges. Low-field MRI, operating at magnetic field strengths of around 0.5 T [2], opens up possibilities for combining these two techniques. By matching the US frequency to the Larmor frequency, the characteristic frequency at which nuclear spins precess in a magnetic field in NMR, relaxation processes can potentially be modulated. This could result in enhanced tissue contrast in MR images.

One of the relaxation processes that is of particular interest in the context of acoustic modulation is the longitudinal or T_1 relaxation [3, 4]. Modulating longitudinal relaxation rates using US waves has been a field of research since 1952, first introduced by Kastler [5]. This field is often referred to as Nuclear Acoustic Resonance (NAR) or Acoustic Nuclear Magnetic Resonance (ANMR). In solids, positive results for ANMR measurements were obtained by Kastler, Al'Tshuler [6] and Proctor and Tantila [7], where mainly paramagnetic crystals were used. However, in liquids, which are more similar to biological tissue, the effect of acoustic waves on longitudinal relaxation produced conflicting results. While some studies, such as Bowen's in 1966 [8], reported null effects in various aqueous solutions, others reported measurable modulation effects [9, 10].

The findings from Bowen were supported by Vuong et al. who used the semi-classical Redfield theory to explain the conflicting ANMR results [11]. In this paper, the authors note that for the US wave to contribute sufficiently to a change in spectral density, two conditions need to be met: 1) resonance, meaning that the US frequency must be equal to the Larmor frequency, and 2) the spin system must have a correlation time which is greater than or equal to the US period. The correlation time refers to the timescale of the thermal motion, which for small particles like water is much smaller than the US period. The authors conclude that these conditions can be met by suspending larger magnetic particles, such as superparamagnetic iron oxide nanoparticles (SPIONs), in a sample to match the US period to the correlation times. Consequently, a study by Mende et al. from 2009 demonstrated that piezoelectric nanoparticles can facilitate US modulation of relaxation rates in liquids [12].

In 2010 and 2011, two theses on the effect of resonant US on the longitudinal relaxation rate in aqueous colloidal suspensions containing SPIONs were published by Höhl and Elmiladi from the University of Bonn, Germany [13, 14]. These highlight the importance of asymmetrical SPIONs. Due to the periodicity of the US wave, an additional rotational oscillation of the asymmetrical particle is expected on top of the thermal motion, resulting in a more effective relaxation rate modulation.

Building on the findings of Höhl and Elmiladi, further research into the dynamics of SPIONs under US waves is necessary to analyze the contributions of rotational and translational motion. Therefore, the aim of this work will be twofold. Firstly, a theoretical description of SPION cluster dynamics under the influence of US waves will be developed to estimate the effect of rotational and translational motion on the fluctuation in the local magnetic dipole field, thereby offering unique insights into their respective contribution to relaxation mechanisms in ANMR. Secondly, experimental ANMR measurements will be conducted on three aqueous SPION suspensions with particle diameters of 50, 130, and 300 nm to research the effect of particle size on the longitudinal relaxation rate.

If successful, this research could introduce a novel contrast mechanism for low-field MRI by utilizing US to enhance MR image contrast. Furthermore, the wide range of surface coating options for SPIONs enables targeted delivery to specific tissues [15], which could offer localized contrast enhancement.

Theory

2.1. Nuclear Magnetic Resonance

2.1.1. Nuclear Magnetism

Nuclear Magnetic Resonance (NMR) is a physical phenomenon in which atomic nuclei are exposed to a strong external magnetic field. Many nuclei possess an intrinsic angular momentum known as spin, which gives rise to a magnetic dipole moment (μ) following [3]:

$$\mu = \gamma \hbar I \tag{2.1}$$

Here, $\hbar I$ is the spin angular momentum, with \hbar being the reduced Planck's constant $\hbar = \frac{\hbar}{2\pi}$ and I being the spin quantum number. The proportionality constant γ is the gyromagnetic ratio, which is specific to each nuclear species. In an external magnetic field (B_0) , hydrogen nuclei (protons), which have a non-zero spin, will align either parallel or antiparallel with the magnetic field. This results in a lower energy state, where the spins align with B_0 , and a higher energy state where the spins align opposite to B_0 . This effect is called the Zeeman effect [16], which is illustrated in Figure 2.1.

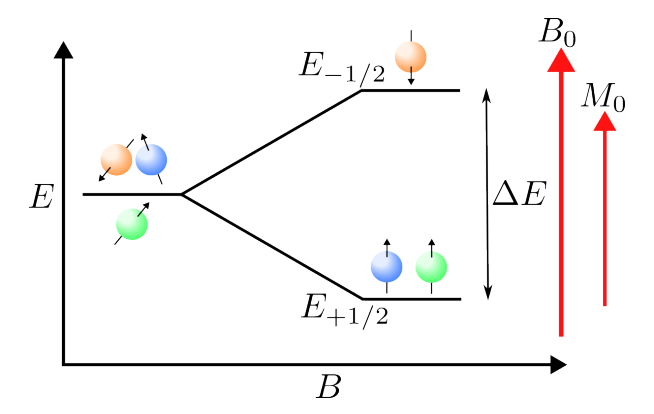


Figure 2.1: The Zeeman effect illustrated for a two-level spin system, such as the proton nuclei in NMR. Black arrows indicate magnitudes, and red arrows indicate direction. Here, the energy is on the y-axis, and the magnitude of the external magnetic field is on the x-axis. Once the magnetic field (B_0) is applied, the majority of the hydrogen nuclei will align with the magnetic field, splitting the energy levels into a lower state $(E_{+1/2})$ and a higher state $(E_{-1/2})$, resulting in a net magnetization (M_0) in the same direction as B_0 . Note that if the magnitude of the external field (B) is increased, the difference between the energy levels (ΔE) and the magnitude of M_0 will increase as a result.

The energy of the spin state (E_m) can be described as follows [3]:

$$E_m = -m\gamma\hbar B_0 \tag{2.2}$$

where m=I,I-1,...,-I indicates the spin magnetic quantum number. For protons, the spin quantum number I=1/2, so m=1/2 and m=-1/2, resulting in an energy difference ΔE between the two levels of:

$$\Delta E = E_{-1/2} - E_{+1/2} = \gamma \hbar B_0 \tag{2.3}$$

This equation highlights the proportionality between the difference in energy level and the external magnetic field, which is also illustrated in Figure 2.1. The larger the magnetic field, the larger ΔE . Since the low-energy state is more energetically favourable, more protons will be in the lower energy state, resulting in a net magnetization (M_0) in the same direction as the external field. The net magnetization component along B_0 is called the longitudinal magnetization.

As a result of the external magnetic field, the net magnetization will precess around the axis of the magnetic field. The frequency of precession is called the Larmor frequency. For an energy difference ΔE (Equation 2.3) between the two spin states and with $\Delta E = h\nu_0$, with ν_0 being the photon frequency, the Larmor frequency ω_0 is defined as:

$$\omega_0 = \gamma B_0 \tag{2.4}$$

2.1.2. Principles of NMR

In nuclear magnetic resonance (NMR), the net magnetization of a sample is much weaker than the external magnetic field B_0 . To generate a detectable signal, the net magnetization must be tipped away from the B_0 axis. This is accomplished by applying a radio frequency (RF) pulse that excites the nuclei. The energy of the RF pulse is absorbed most efficiently under the resonance condition, meaning the RF frequency exactly matches the Larmor frequency corresponding to the energy difference ΔE .

In the configuration of an external magnetic field B_0 oriented along the z-axis, the longitudinal magnetization M_z aligns in the direction of B_0 (Figure 2.2a). For an ideal 90° RF pulse, M_z is fully converted into transverse magnetization M_{xy} , which is the magnetization in the xy-plane (Figure 2.2b). The precession of M_{xy} around B_0 induces a signal in the NMR receiver coils, allowing it to be measured via the Lorentz principle. This signal is known as the Free Induction Decay (FID).

After the RF pulse, the longitudinal magnetization will regrow to its equilibrium state as a result of many interactions between the nuclei and their surroundings. This process is known as longitudinal relaxation and is characterized by the time constant T_1 . Concurrently, the transverse magnetization will decay to its original state due to the loss of phase coherence between the individual spins. This is primarily caused by interactions which occur when the magnetic moment of one spin influences the local magnetic field of other nuclei [17]. This process is called transverse relaxation and is characterized by a time constant T_2 . These relaxation processes, as illustrated in Figure 2.2c, govern the signal intensity in both NMR and MRI, as they determine how quickly the magnetization in a specific sample returns to its equilibrium state.

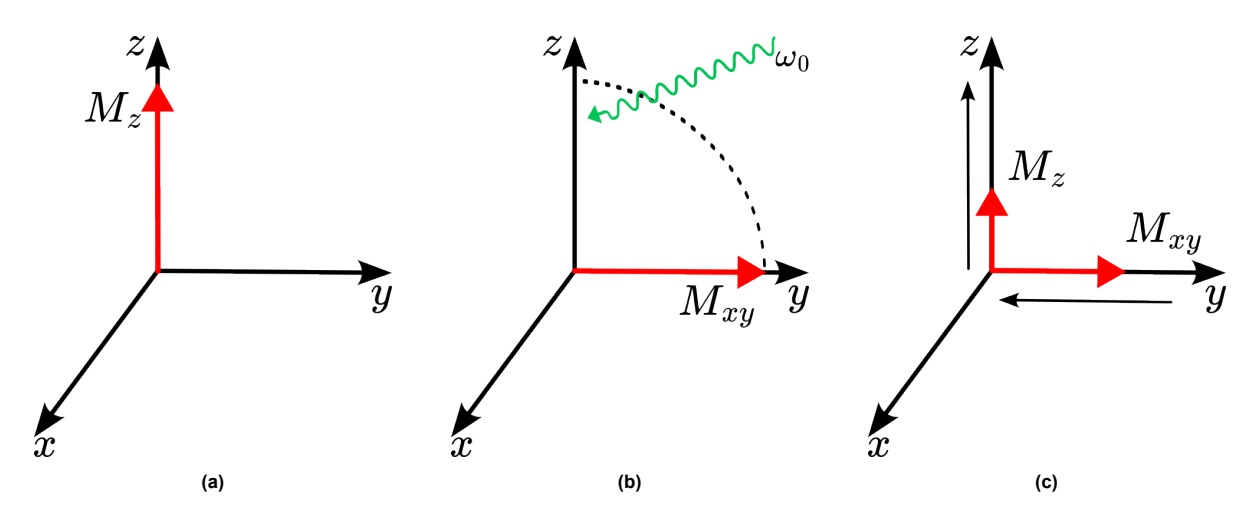


Figure 2.2: Visualization of the behaviour of net magnetization in NMR in the rotating frame of reference. (a) In the presence of an external magnetic field B_0 , the net magnetization M_0 aligns along the z-axis, creating longitudinal magnetization M_z . (b) Upon application of an ideal 90° RF pulse at the Larmor frequency ω_0 , M_z is fully converted into transverse magnetization M_{xy} in the xy-plane, where it precesses around B_0 and generates the detectable NMR signal. (c) After the RF pulse, M_z regrows toward equilibrium through longitudinal relaxation, while M_{xy} decays due to transverse relaxation.

In reality, T_2 is most often accompanied by concurring processes such as field inhomogeneities and susceptibility differences [17, 18]. These processes are often combined into an additional term T_2' and lead to an apparent decrease in T_2 according to:

$$\frac{1}{T_2^*} = \frac{1}{T_2} + \frac{1}{T_2'} \tag{2.5}$$

Here, T_2^* describes the effective T_2 time.

2.1.3. Relaxation and Bloch equations

In 1946, Felix Bloch proposed a set of equations for the description of the dynamics of the net magnetization of an ensemble of nuclei subjected to an external magnetic field [19]. Using the equation of motion for the magnetic moment in a homogeneous magnetic field, which is described as:

$$\frac{dM}{dt} = \gamma M \times B \tag{2.6}$$

It is assumed that the relaxation terms can be superimposed on the equation of motion [3], resulting in:

$$\frac{dM}{dt} = \gamma (M \times B) - \frac{M_x \hat{x} + M_y \hat{y}}{T_2} - \frac{(M_z - M_0)\hat{z}}{T_1}$$
 (2.7)

Here, M is the magnetic moment vector, B is the applied magnetic field vector, and $(\hat{x}, \hat{y}, \hat{z})$ are the unit vectors. M_0 is the initial net magnetization. After the RF pulse at t=0, the longitudinal magnetization $M_z(0)$ and transverse magnetization $M_{xy}(0)$ will follow an exponential described as:

$$M_z(t) = M_z(0)e^{-t/T_1} + M_0(1 - e^{-t/T_1})$$
 (2.8)

$$M_{xy}(t) = M_{xy}(0)e^{-t/T_2} (2.9)$$

In a FID measurement, the detected signal (s(t)), which is proportional to the transverse magnetization M_{xy} , is described by:

$$s(t) \propto M_{xy}(0)e^{-t/T_2^*}$$
 (2.10)

2.1.4. Relaxation mechanisms

Longitudinal relaxation and transverse relaxation both arise from interactions between nuclei and their surrounding environment. At the microscopic level, these interactions are driven by time-dependent fluctuations in the local magnetic field generated by the nuclei, which are primarily caused by thermal motion effects [20]. These thermal motion effects include rotation and translation and can often be described as stochastic processes. The stochastic motion perturbs the nuclear dipolar interactions, resulting in increased nuclear energy exchange and dephasing.

In 1948, Bloembergen, Purcell, and Pound proposed the so-called Bloembergen-Purcell-Pound theory (BPP theory), which can be used to determine the relaxation rate that arises from the local magnetic field fluctuations as a result of molecular motion [21]. The BPP theory models the relaxation rate using an autocorrelation function, which describes how the position of particles at time t is correlated to their position at time τ . According to the BPP theory, the autocorrelation function (G(t)) is a decaying function over time and is proportional to e^{-t/τ_c} , with τ_c being the correlation time that reflects the characteristic timescale of molecular motion, which is proportional to the cubed radius of the molecule.

Correlation times can be split into rotational and translational correlation times. The Stokes-Einstein-Debye and the Stokes-Einstein equations provide the necessary information for calculating the rotational-and translational correlation times, respectively [22]. The rotational correlation time $\tau_{c,r}$ is determined using the rotational diffusion coefficient D_r as a function of the hydrodynamic radius of the particle r_H and the dynamic viscosity η .

$$D_r = \frac{k_B T}{8\pi \eta r_H^3}, \quad \tau_{c,r} = \frac{1}{6D_r} = \frac{4\pi \eta r_H^3}{3k_B T} \tag{2.11}$$

The translational correlation time $\tau_{c,t}$ is determined using the translational diffusion coefficient D_t .

$$D_{t} = \frac{k_{B}T}{6\pi\eta r_{H}}, \quad \tau_{c,t} = \frac{r_{H}^{2}}{D_{t}} = \frac{6\pi\eta r_{H}^{3}}{k_{B}T}$$
 (2.12)

If molecules rotate and translate at high frequencies, the correlation at τ is low, whereas the correlation is high at τ for larger molecules with longer τ_c , as illustrated in Figure 2.3.

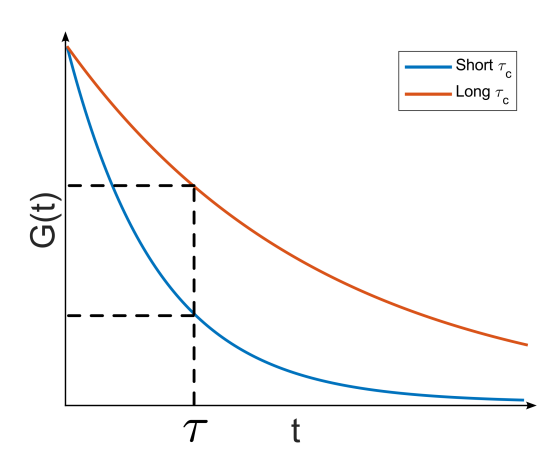


Figure 2.3: Illustration of the correlation function G(t) shown for two molecules of short and long correlation times (τ_c). Large molecules have longer correlation times, resulting in larger correlation values at time τ , while smaller molecules with shorter τ_c show lower correlation.

This information contained in the autocorrelation function can then be used to determine the longitudinal relaxation time T_1 as a function of the spectral density $J(\omega)$, which is the Fourier transform of the correlation function.

2.2. SPIONs 7

$$\frac{1}{T_1} = C \cdot \left[\frac{\tau_c}{1 + \omega_0^2 \tau_c^2} + \frac{2\tau_c}{1 + 4\omega_0^2 \tau_c^2} \right]$$
 (2.13)

Here, $C=\frac{3\mu_0^2\hbar^2\gamma^4}{160\pi^2d^6}$ for protons, with μ_0 being the magnetic permeability of free space and d the distance between the two dipoles. Note that the Fourier transform of e^{-t/τ_c} is equal to $J(\omega_0)=\frac{\tau_c}{1+\omega_0^2\tau_c^2}$. Equation 2.13 suggests that the inverse of the relaxation time T_1 , also known as the relaxation rate R_1 , is closely tied to the spectral density $J(\omega_0)$. Notably, R_1 reaches a maximum when the characteristic frequency of molecular motion equals the Larmor frequency $(1/\tau_c\approx\omega_0)$. This highlights a critical point: when molecular motion occurs at ω_0 , it most effectively stimulates longitudinal interactions, thereby shortening the T_1 relaxation time.

2.2. SPIONs

As highlighted previously, the interactions between nuclei in a sample are one of the key factors influencing the relaxation rate. Since T_1 and T_2 are inherent, tissue-specific properties, this phenomenon is widely used in MRI to generate image contrast. A great example is the difference in T_1 between water and fat. Water contains many small molecules with a short τ_c , where the molecular motion is faster than the Larmor frequency, leading to less efficient interactions and longer T_1 times. Fat tissue, on the other hand, contains many long-chain triglycerides with relatively long τ_c that better match the Larmor frequency, resulting in many efficient interactions and shorter T_1 times. As a result, fat and water components will be subject to different degrees of T_1 recovery for a certain sequence timing, leading to different signal intensities in the image.

To further enhance MRI image contrast, contrast agents, like Gadolinium-based compounds or Superparamagnetic Iron Oxide Nanoparticles (SPIONs), can be used. These contrast agents, having τ_c in the range of ω_0 and stronger local magnetic field fluctuations [23], can greatly enhance interactions, resulting in shortened T_1 or T_2 values. The induced increase in relaxation rate is directly proportional to the concentration C of the contrast agent. This dependence can be described through the relaxivity r_i , which is defined as the change in relaxation rate per unit concentration [17]:

$$R_i = \frac{1}{T_i} = \frac{1}{T_{i,0}} + r_i C$$
 (2.14)
= $R_{i,0} + r_i C$ with $i = 1, 2$.

Due to their high relaxivity, SPIONs have been used as in vivo contrast agents for shortening transverse relaxation times in MRI [24]. These may offer an alternative to avoiding certain risks associated with conventional gadolinium-based agents [15, 25]. SPIONs are synthetic maghemite (γ -Fe₂O₃) or magnetite (Fe₃O₄) particles with core sizes ranging from around 5 to 100 nm in diameter, corresponding to correlation times between 25 ns and 200 μ s [9].

The superparamagnetic property of SPIONs refers to the ability of the particle to reach saturation magnetization if an external magnetic field is turned on without exhibiting residual magnetization when the external field is removed [15]. Below a certain critical size, SPIONs consist of a single magnetic domain. When the core size of the SPION exceeds this critical size, the superparamagnetic behaviour disappears, weakening the response of the SPION to an external magnetic field. In general, the critical size for a spherical SPION containing a magnetite core is around 25 nm [26].

Although most SPIONs are spherical, they can exhibit anisotropic shapes, such as rods, films, cubic, and nanoflowers [27]. SPIONs can be coated with a variety of molecules, ranging from starch-based coatings to gold coatings. These coatings allow the SPIONs to form a stable colloid and attach therapeutic molecules, enabling site-specific drug delivery by improving solubility and biocompatibility. Furthermore, coatings can reduce the tendency to aggregate, protect the core from oxidation, and allow the conjugation of targeting ligands [15].

2.3. Ultrasound and particle dynamics

Ultrasound (US) refers to sound waves with frequencies above the human hearing range, which is approximately greater than 20 kHz. US waves are mechanical vibrations in a medium that create pressure variations. Sound waves show longitudinal behaviour, meaning that the oscillations of the wave occur in the same direction as the wave propagation [28]. In this section, the basics of US and the equations governing particle motion in an US field will be explained.

2.3.1. Basics of US

In medical applications, the propagation velocity of US waves in tissue is often approximated to be equal to the velocity of US waves in water, which is around 1500 m/s. The speed of sound c, wavelength λ and frequency f are related by the equation:

$$c = \lambda f \tag{2.15}$$

Furthermore, the speed of sound also depends on the type of medium as follows:

$$c = \sqrt{\frac{1}{\rho\kappa}} \tag{2.16}$$

Here, ρ is the density and κ is the compressibility of the medium. In the instance of a sound wave with pressure amplitude P and angular frequency ω of the form:

$$p(t) = P\cos(\omega t) \tag{2.17}$$

The particles in the medium moved by that sound wave have a velocity $v=\frac{P}{Z_a}$, with $Z_a=\rho c$ being the acoustic impedance of the medium. The acoustic impedance is a medium-dependent constant that reflects the resistance that an ultrasound wave encounters when traveling through a medium [29].

2.3.2. Particle dynamics

Based on the above relations, the particle displacement ζ for a plane wave, approximated far away from the acoustic source, can be expressed by [29]:

$$\zeta = \frac{p(t)}{\omega \rho c} \tag{2.18}$$

Important to note is the proportionality between displacement and pressure, and the inverse relation between the displacement and frequency as shown in Figure 2.4, where the displacement over time for water molecules is shown.

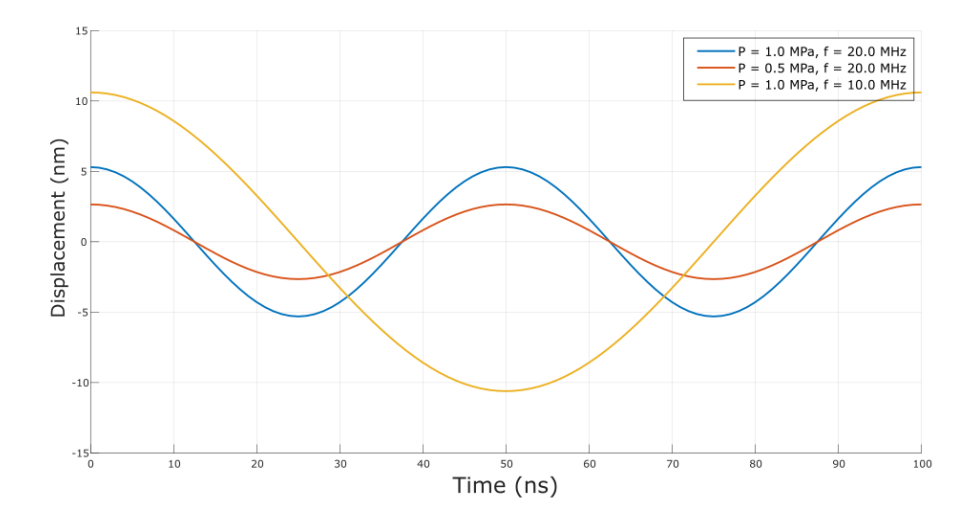


Figure 2.4: Simulated displacement of a water molecule over time for ultrasound waves with pressure $p(t)=P\cos(\omega t)$ calculated with Equation 2.18. This figure illustrates the proportionality between the pressure and displacement, as well as the inverse relationship between frequency and displacement. Blue: P=1.0 MPa, f=20.0 MHz. Orange: P=0.5 MPa, f=20.0 MHz. Yellow: P=1.0 MPa, f=10.0 MHz

The displacement for SPIONs in a medium is determined differently, as SPIONs exhibit a higher density and lower compressibility than water particles. To determine the dynamics of SPIONs, the force generated by the US field on the SPIONs should be determined. This force is called the instantaneous force. In general, the instantaneous force experienced by a particle in an acoustic field depends on the pressure gradient $\nabla p(t)$ and the volume of the particle $V_p(t)$ [30], and is given by:

$$F(t) = -V_p(t)\nabla p(t) \tag{2.19}$$

In applications such as acoustophoresis, a description of the net motion of a particle, called the acoustic radiation force, is required. This force is a time-averaged instantaneous force and is dependent on specific particle properties, such as its density and compressibility. A derivation for the acoustic radiation of a standing wave is provided in Appendix A. Unlike Equation A.3 and A.4, the equation for the instantaneous force retains its time dependence and allows for modeling of the oscillatory behaviour of SPIONs at the US driving frequency. For a one-dimensional progressive acoustic wave with angular frequency ω of the form:

$$p(x,t) = P_a \cos(kx - \omega t) \tag{2.20}$$

The corresponding pressure gradient is given by:

$$\nabla p(t) = \frac{\partial p(x,t)}{\partial x} = -kP_a \sin(kx - \omega t)$$
 (2.21)

F(t) can then be written as:

$$F(t) = V_p(t)kP_a\sin(kx - \omega t) \tag{2.22}$$

Even though SPIONs are highly incompressible¹, their slight volume pulsation and oscillatory movement in the acoustic field generate a second-order component as described in Appendix A. This produces a non-zero average force over time, resulting in both an oscillatory and a net motion of the particle.

Gires et al. (2018) have proposed a theoretical framework for the instantaneous acoustic force of a standing wave, where it is shown that averaging the instantaneous force leads to the same equation as Equation A.3 [31]. However, because of the low compressibility and the fact that only the magnitude of the short-term motion of the particle is important in this research, the second-order component of the instantaneous acoustic force can be neglected. This allows the use of Equation 2.19 to model the dynamics of the SPIONs in the acoustic field under the assumption that $V_p(t) \approx V_p$, which will further be described in chapter 3.

2.4. The principles of Acoustic NMR

Acoustic NMR (ANMR) is a variation of conventional NMR techniques that utilizes US waves to modulate longitudinal relaxation mechanisms [4]. The main goal of ANMR is to stimulate fluctuations in the local magnetic field by applying an US pulse resonant with the Larmor frequency, thereby providing an additional pathway for energy exchange between nuclei and the lattice.

When molecular tumbling rates, characterized by the correlation time τ_c , predominantly occur at Larmor frequency, relaxation processes are most efficient. If τ_c is much shorter than the US period, the timescale of the motion of small molecules typically does not align with the period of the US wave. As a result, the US wave is unable to efficiently couple to this high-frequency motion, and the induced magnetic field fluctuations at the Larmor frequency are minimal [11]. More precisely, for US frequencies around 20 MHz and small molecules like water, Brownian motion is the dominant contributor to relaxation rates as the US period is much longer than the timescale of this motion. This effect is illustrated in Figure 2.5. For small particles such as water molecules, the fluctuations in the local magnetic field experienced by a proton (dark red) as a result of relative motion to other particles decay already within the period of the US wave, limiting sufficient US coupling. In contrast, larger particles such as SPIONs exhibit a longer correlation time of around 25 ns to $200~\mu s$. Therefore, the correlation of the magnetic field fluctuations caused by the relative motion between the SPION and a nearby proton decays more slowly compared to the case without SPIONs.

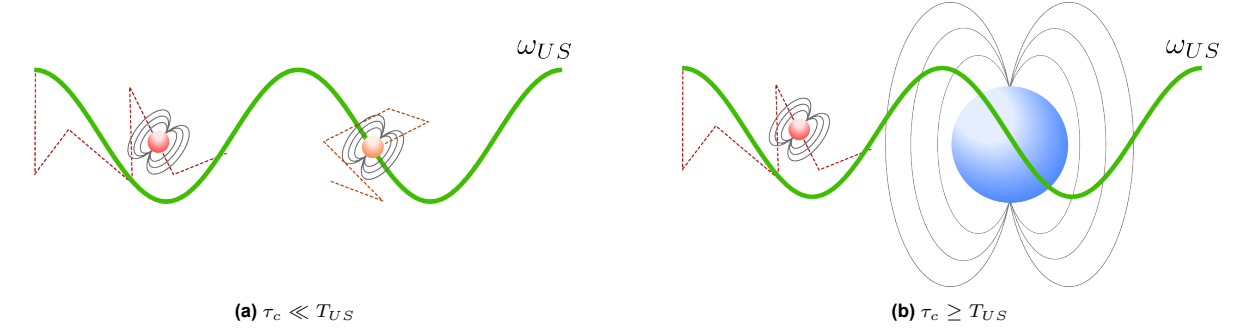


Figure 2.5: Illustration of the effect of US on the local magnetic field fluctuations in Acoustic NMR. (a) In water, where $au_c \ll T_{US}$, the correlation of the experienced local magnetic field of a proton (dark red) decays too quickly for US waves to efficiently couple. (b) In SPION solutions with $au_c \geq T_{US}$, the experienced magnetic field by the proton remains coherent for a longer period, allowing the US wave to induce sufficient local magnetic field fluctuations at the Larmor frequency. Particle and wave sizes are exaggerated for clarity.

So far, no theoretical framework for the relaxation rate under the influence of US irradiation has been established, which considers the dipolar interaction between SPIONs and water protons. This is mainly due to the difficulty of determining the rate of interactions between particles. However, for water protons only, a theoretical framework was proposed by Vuong et al. in 2008 [11]. Here, the authors attempt to calculate the spectral density directly, as was proposed by Bowen (1964) [32]. The increment in the spectral density function due to the presence of the US wave is given by:

$$\Delta J^{(m)}(\omega_I) = \left(\frac{A}{\omega d}\right)^2 \frac{4s_n N \tau_D}{15d^3} M_m(\omega \tau_D, \omega_I \tau_D)$$
(2.23)

Where A is the amplitude of the US wave in m/s, ω is the angular US frequency, ω_I is the proton Larmor

frequency, s_n is a spherical harmonic function, N is the mean number of interacting spins, and $\tau_D=d^2/D$, with d being the distance between spins and D being the diffusion coefficient. $M_m(\omega\tau_D,\omega_I\tau_D)$ models the effect of ultrasound frequency and proton Larmor frequency on the spectral density that shows a maximum value at $\omega=\omega_I$. Using Equation 2.23, an upper bound for the relative change in spectral density due to US waves can then be defined as:

$$\frac{\Delta J^{(0)}(0)}{J^{(0)}(0)} < 0.05 \left(\frac{15}{4\pi}\right) \left(\frac{\tau_D}{d/A}\right)^2 \frac{1}{\sqrt{\omega \tau_D}} \tag{2.24}$$

For water molecules with A=0.01 m/s and an US frequency of 20 MHz, the term $\left(\frac{\tau_D}{d/A}\right)^2$ will be on the order of 10^{-7} and the term $\frac{1}{\sqrt{\omega\tau_D}}$ will be on the order of 10^1 , resulting in a relative spectral density increment of 10^{-8} . However, for SPIONs with a correlation time of $\tau_D=R^2/D$, the relative spectral density can theoretically increase by values of 10^{-2} to 10^{-1} , indicating a substantial change in spectral density due to the influence of US. The corresponding numerical estimates are compiled in Table 2.1.

Table 2.1: Numerical values of the different terms from Equation 2.24 and their product. Calculations are shown for water molecules and for SPIONs of different radii (5–100 nm) at an ultrasound amplitude A=0.01 m/s and frequency 20 MHz.

Particle	Radius (nm)	$\left(rac{ au_D}{d/A} ight)^2$	$rac{1}{\sqrt{\omega au_D}}$	$0.05\left(rac{15}{4\pi} ight)\left(rac{ au_D}{d/A} ight)^2rac{1}{\sqrt{\omega au_D}}$
Water molecule	0.14	$5.44 \cdot 10^{-8}$	26.7	$2.61 \cdot 10^{-8}$
SPION	5	$2.78 \cdot 10^{-4}$	2.45	$1.22 \cdot 10^{-5}$
	25	0.17	0.49	$1.2 \cdot 10^{-3}$
	65	7.93	0.19	0.027
	150	225	0.08	0.33

2.5. Asymmetrical SPIONs

In 2010 and 2011, two theses on the effect of resonant US on the longitudinal relaxation rate in aqueous colloidal suspensions containing SPIONs were published by Höhl and Elmiladi from the University of Bonn, Germany [13, 14]. These theses highlight the importance of asymmetrical SPIONs, showing that asymmetrical SPIONs produced by coating the SPION with antibodies show a decrease in T_1 . The influence of the rotational motion of asymmetrical SPIONs on the fluctuations in the local magnetic field is illustrated in Figure 2.6. Due to the periodicity of the US wave, symmetrical SPIONs will show mostly translational motion and Brownian motion. However, for asymmetrical particles, an additional rotational oscillation is expected. Due to the addition of fluctuation of the local magnetic field, additional dipolar coupling is expected under resonance conditions.

It is worth noting that SPION asymmetry does not necessarily arise only from the shape of individual nanoparticles or their coating, but can also result from the formation of aggregates. These aggregates possess non-spherical, anisotropic structures that can induce similar rotational dynamics under US excitation. A review on the formation of SPION aggregates can be found in Appendix B.

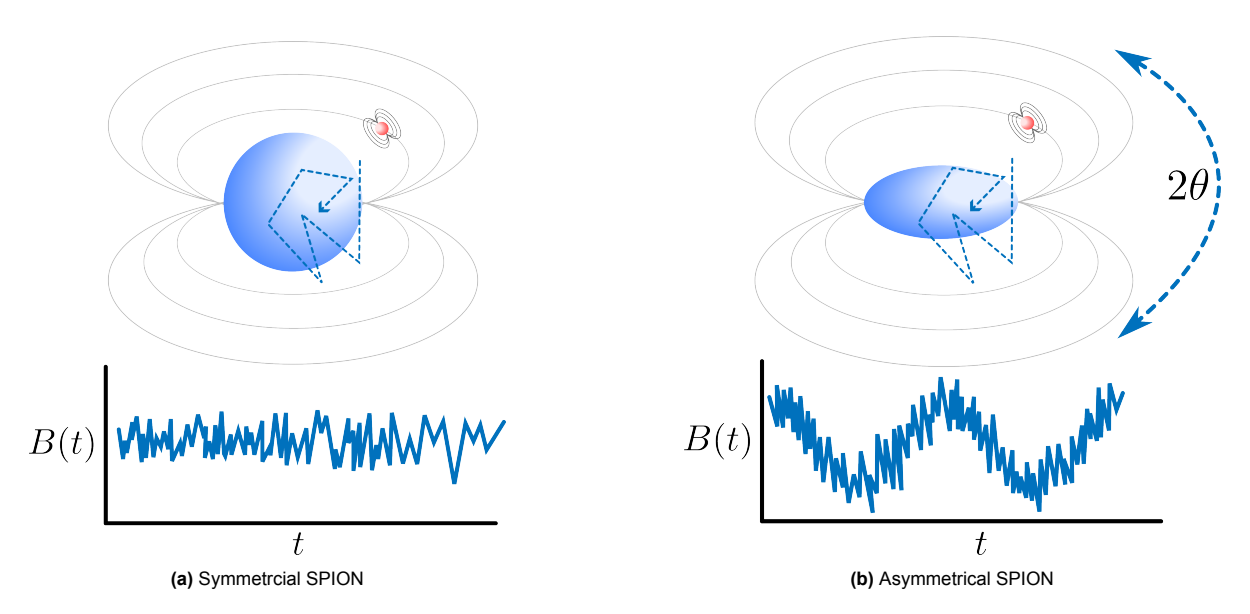


Figure 2.6: Illustration of the effect of SPION asymmetry on the fluctuation in the local magnetic field experienced by a surrounding proton (in red) when subjected to US waves. (a) A symmetrical SPION (in blue) shows mainly translational and Brownian motion, resulting in incoherent local magnetic field fluctuations experienced by the proton. (b) Asymmetrical SPIONs show an additional rotational motion with a maximum angle of 2θ , resulting in local magnetic field fluctuations at the frequency of the US waves.

3

Methods

The focus of this work is twofold: to develop a theoretical description of SPION dynamics and the resulting local magnetic field fluctuations due to US waves, and experimentally evaluate acoustic modulation of T_1 relaxation. The methodological approach to both will be described in this chapter.

3.1. Ultrasound-modulated SPION relaxation model

As relaxation rates are proportional to the spectral density functions, stimulating motion of the SPIONs at the Larmor frequency can enhance relaxation rates of the surrounding water. As SPION clusters are expected to show different dynamics compared to individual SPIONs, it is of great importance to improve the understanding of expected cluster sizes and cluster dynamics when subjected to US waves. The dynamics of the SPION aggregates can then be used to model magnetic field fluctuations, allowing estimation of relaxation rate changes caused by the US wave. The model performs this task by executing the following sequence of steps:

- 1. Create a randomly oriented cluster of N SPIONs in a voxel.
- 2. Use the k-Wave MATLAB toolbox to simulate an acoustic pressure field and define the cluster's position in this pressure field.
- 3. Calculate the resulting force on the cluster using Equation 2.19.
- 4. Using the equations of motion, calculate the translational and rotational dynamics following the Explicit Euler method.
- 5. Determine the local fluctuation in the magnetic field in this voxel.
- 6. Calculate the autocorrelation function and its Fast Fourier transform (FFT).
- 7. Determine the longitudinal relaxation rate in this voxel.

Table 3.1 summarizes the model parameters used in the simulation. These values form the basis of the model calculations described in subsection 3.1.1 to 3.1.6.

Parameter	Description	Value	Unit	Relevant for subsection
R	SPION radius	25	nm	3.1.1
ρ	SPION density	2500	kg/m ³	3.1.1
$\mid \eta \mid$	Dynamic viscosity of water	0.7191×10^{-3}	Pa⋅s	3.1.1
N_{rep}	Number of simulation repititions	1000	-	3.1.1
R_q	Radius of gyration (cluster)	variable	nm	3.1.2
N	Number of SPIONs in cluster	2 - 100	-	3.1.2
k_0	DLCA prefactor	1.3	-	3.1.2
d_f	DLCA fractal dimension	1.78	-	3.1.2
$\int dx$	Spatial resolution	0.01	mm	3.1.3
dt	Time resolution	0.667	ns	3.1.3
x, y	SPION cluster position	0.32, -0.03	mm	3.1.3
M_s	Saturation magnetization of SPION	75	A⋅m ² /kg	3.1.4
r	SPION-proton distance	variable	m	3.1.6 and 3.1.4

Table 3.1: Overview of model parameters used in the simulation.

3.1.1. Equations of motion

Following Newton's second law, both translational and rotational motion of a particle in a moving medium subjected to acoustical waves can be described as follows:

$$ma_p + \zeta_t(v_p - v_m) = F(t) \tag{3.1}$$

$$I\alpha_p + \zeta_r(\omega_p - \omega_m) = \tau(t) \tag{3.2}$$

Here, m and I are the particle's mass and moment of inertia, a_p and α_p its acceleration and angular acceleration, and v_p , v_m , ω_p , and ω_m the velocities and angular velocities of the particle and medium. F(t) and $\tau(t)$ denote the instantaneous force and torque on the particle, where the force has been determined using Equation 2.19. In the above equations, force and torque are opposed by rotational and translational friction coefficients ζ_t and ζ_r , respectively. Here, $\zeta_t = 6\pi\eta R_g$ represents the translational friction coefficient for a sphere of gyration radius R_g , and $\zeta_r = 8\pi\eta R_g^3$ is the rotational friction coefficient. Therefore, in modeling the motion of a SPION cluster in water under the influence of acoustic pressure, the cluster is approximated as a sphere of radius R_g .

The angular velocity of the medium, ω_m , is calculated by considering the vorticity of the medium Ω_m . The vorticity is defined as twice the angular velocity [33]. Assuming a two-dimensional flow in the x-y plane, where x represents depth, y represents width, and any out-of-plane flow in the z-direction is ignored, the vorticity is defined as the curl of the velocity field $\mathbf{v_m}(v_x, v_y)$, described as:

$$\Omega_m = \nabla \times \mathbf{v_m} = \left(\frac{\partial v_y}{\partial x} - \frac{\partial v_x}{\partial y}\right) \tag{3.3}$$

Equation 3.2 then becomes:

$$I\alpha_p + \zeta_r \left(\omega_p - \frac{1}{2}\Omega_m\right) = \tau(t)$$
(3.4)

Based on the pressure field experienced locally by the particle, the forces are computed using Equation 2.19. Assuming that SPION clusters behave as rigid bodies, the resulting torque on the cluster can be calculated as:

$$\tau(t) = \sum_{i=1}^{N} \left[-(y_i - y_c) F_{x,i}(t) + (x_i - x_c) F_{y,i}(t) \right]$$
(3.5)

Here, $F_{x,i}$ and $F_{y,i}$ are the forces in the x and y directions acting on the i^{th} SPION within the cluster, x_i and y_i are its coordinates, and x_c and y_c denote the coordinates of the cluster's center of mass. Note that if N=1, the SPION will exhibit zero torque, as the force experienced locally by the SPION is approximated to be homogeneous inside one voxel. The force and torque on the cluster allow for the estimation of the translational and rotational motion for each time step n with duration Δt of the cluster subjected to the US wave using the explicit Euler method [34] as follows:

$$v_{n+1} = v_n + a_n \Delta t$$

 $x_{n+1} = x_n + v_{n+1} \Delta t$ (3.6)

$$\omega_{n+1} = \omega_n + \alpha_n \Delta t$$

$$\theta_{n+1} = \theta_n + \omega_{n+1} \Delta t$$
(3.7)

Here, a_n and α_n at the current time step can be determined from Equation 3.1 and 3.4 and are given by:

$$a_n = \frac{\sum_{i=1}^{N} [F_i(t)] - \zeta_t(v_p - v_m)}{m}$$
(3.8)

$$\alpha_n = \frac{\tau(t) - \zeta_r \left(\omega_p - \frac{1}{2}\Omega_m\right)}{I} \tag{3.9}$$

In this way, both the translational and rotational dynamics of a SPION cluster are determinable using viscous drag, inertia and mass, and the force and torque. This process was repeated $N_{rep}=1000$ times, from which the average value and variability of the maximal rotational and translational displacements were determined.

3.1.2. Cluster size

With a model for the motion in place, the next step is to describe the cluster properties that influence these dynamics, such as size and drag. A recent study suggests that SPION aggregation can be described as diffusion-limited cluster aggregation (DLCA), which means that SPIONs cluster as a result of Brownian motion, leading to aggregates with fractal dimensions [35]. DLCA's follow the following relationship:

$$N = k_0 \left(\frac{R_g}{R}\right)^{d_f} \tag{3.10}$$

where N is the number of SPIONs in the cluster, R is the radius of a single SPION, R_g is the radius of gyration of the cluster, and k_0 and d_f are the prefactor and the fractal dimension, respectively [36]. The larger d_f , the denser the cluster is [37]. For SPION aggregates, k_0 typically ranges from 1.2 to 2.0 and d_f from 1.6 to 2.2 [35].

This equation can be used to estimate the size and shape of the cluster as determined by R_g and d_f , respectively. However, estimating the number of SPIONs in a cluster is impossible when R_g is unknown. One study suggests that 50%-80% of the SPION clusters are organized in dimers or trimers [38], while other studies suggest the possibility of the formation of "superaggregates" consisting of more than 10^3 SPIONs [35]. A review on the cause of aggregate formation is presented in Appendix B.

For DLCA clusters, the translational and rotational drag coefficients can be described by the following equations [36, 39].

$$\zeta_t = \zeta_{t,s} \left(\frac{1 + 1.612Kn}{C_t(Kn)} \right) \times \left[\frac{1}{0.852N^{0.535} + 0.148} + \frac{1.612Kn}{0.843N^{0.939} + 0.157} \right]^{-1}$$
(3.11)

$$\zeta_r = \zeta_{r,s} \left(\frac{1 + 5.988Kn}{C_r(Kn)} \right) \times \left[\frac{1}{0.713N^{1.63} + 0.287} + \frac{5.988Kn}{1.184N^{2.02} - 0.184} \right]^{-1}$$
(3.12)

Here, $\zeta_{t,s}=6\pi\eta R$ represents the translational friction coefficient for a sphere given by Stokes' law, and $\zeta_{r,s}=8\pi\eta R^3$ is the rotational friction coefficient for a sphere described in the Stokes-Einstein-Debye relation. C_t and C_r are correction factors. Kn is known as the Knudsen number, which is a dimensionless ratio between the mean free path and the characteristic length [36]. With a mean free path length in water of around 0.3 nm and a SPION of 50 nm diameter, the Knudsen number is approximately equal to $6\cdot 10^{-3}$, meaning that the correction factors in Equation 3.11 and 3.12 vanish, resulting in $\zeta_t \approx \zeta_{t,s}$ and $\zeta_r \approx \zeta_{r,s}$. This justifies the earlier approximation of the cluster as a sphere with a gyration radius R_g in the equations of motion.

3.1.3. k-Wave toolbox

For the simulation of the acoustic pressure field and its gradient $\nabla p(t)$, k-Wave, a MATLAB toolbox designed for time-domain simulation of acoustic fields, can be used [40]. This toolbox allows the computation of acoustic pressure fields for any type of transducer. Since the k-Wave toolbox directly provides v_m but not ω_m , the angular velocity of the medium is derived from the velocity field using Equation 3.3.

A simulated acoustic pressure field using the k-Wave toolbox for a focused transducer with US frequency of 20 MHz and an acoustic pressure of 1 MPa in water, and a randomly generated cluster containing N=12 SPIONs is shown in Figure 3.1. The acoustic attenuation was modeled with a power law of the form $\alpha(f)=\alpha_0\cdot f^y$, with α_0 and y representing the attenuation coefficient in dB/(MHz · cm) and the frequency power law exponent, respectively. The dynamics of the SPION cluster are simulated as if it were located in the position of the red square, where it is assumed that $R_g\ll \lambda$, with λ being the US wavelength.

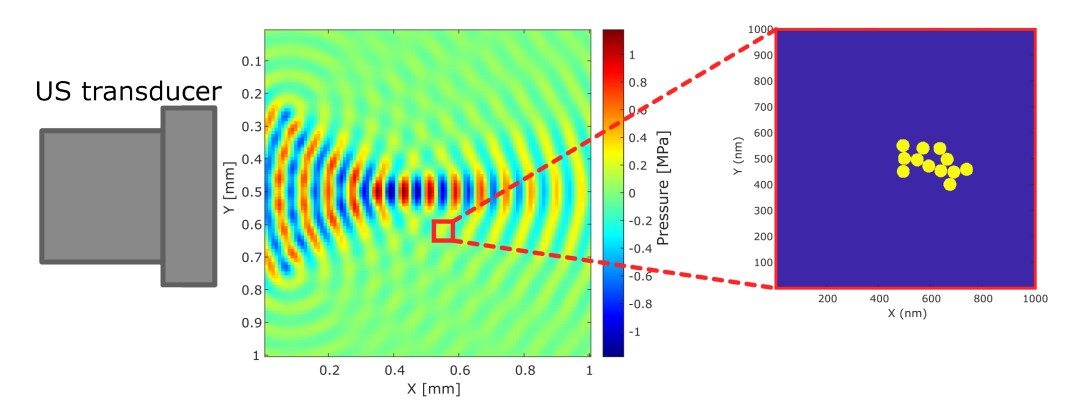


Figure 3.1: A simulated acoustic pressure field using the k-Wave MATLAB toolbox for a focused transducer with US frequency of 20 MHz and an acoustic pressure of 1 MPa in water. The sound waves are traveling in the A randomly generated cluster containing N=12 SPIONs, each with a radius of 25 nm, of which its motion is simulated as if it were located in the red square.

3.1.4. Local magnetic field fluctuations

Once the SPION cluster dynamics are determined, it is now possible to compute the local magnetic field fluctuations using the magnetic dipole field equation [41] given by:

$$B(r,t) = \frac{\mu_0}{4\pi r^3} \left[3(\vec{m}(t) \cdot \hat{r})\hat{r} - \vec{m}(t) \right]$$
 (3.13)

Here, μ_0 is the vacuum magnetic permeability, B is the magnetic field, r is the distance from the SPION to a proton with \hat{r} being the corresponding unit vector, and \vec{m} is the time-dependent magnetic moment vector of the SPION. In the proposed model, the initial direction of the magnetic moment vectors of the SPIONs is defined such that half of the SPIONs' magnetic moments are pointing in the +x direction, while the other half are pointing in the -x direction. Due to the strong magnetization, individual SPIONs

can be approximated as point dipoles with a magnetic moment magnitude of $m=M_sV$, where M_s is the saturation magnetization and V is the volume of the magnetic core of the SPION.

To compute the magnetic field fluctuations, a grid of proton positions each separated by 5 nm is defined surrounding the SPION cluster, excluding grid points that fall within the SPION cores. For each grid point, the distance r to every SPION is calculated, and the dipole field contribution is determined using Equation 3.13. The total magnetic field fluctuation is then determined by summation over the contribution from every SPION. This process is repeated for every grid point, meaning that the size of B(r,t) matrix will be (Q,N_t) , with Q being the number of grid points, and N_t being the number of time steps.

3.1.5. Autocorrelation function

Based on Equation 3.13, the autocorrelation function can be computed. The equation for the autocorrelation as a function of the local magnetic field is defined as [42]:

$$G(\tau) = \langle B(t)B(t+\tau)\rangle_t \tag{3.14}$$

where $\langle \cdot \rangle$ is a time average and τ is the lag time.

3.1.6. Determination of R_1

The longitudinal relaxation rate is proportional to the spectral density at the Larmor frequency and twice the Larmor frequency, meaning that if the motion of SPIONs is increased at the Larmor frequency, longitudinal relaxation rates will be higher. The equation for the longitudinal relaxation rate ($R_1 = 1/T_1$) of spin-1/2 particles is defined as [3]:

$$1/T_1 = \frac{9\gamma^4\hbar^2}{8r^6} \left(\frac{\mu_0}{4\pi}\right)^2 \left[J^{(1)}(\omega_0) + J^{(2)}(2\omega_0)\right]$$
 (3.15)

Here, $J(\omega)$ is the spectral density, which is determined by performing the Fast Fourier transform (FFT) on Equation 3.14, and T_1 is the longitudinal relaxation time. Since the local magnetic field fluctuation, and thus the spectral density function, is evaluated for every individual proton, the total relaxation rate due to US $R_{1,tot}$ in the voxel is then calculated by the summation over all individual proton contributions, as depicted in Equation 3.16.

$$(1/T_1)_{tot} = R_{1,tot} = \sum_{j=1}^{Q} \left(\frac{9\gamma^4\hbar^2}{8r_j^6} \left(\frac{\mu_0}{4\pi} \right)^2 \left[C_Q \cdot \left(J_j^{(1)}(\omega_0) + J_j^{(2)}(2\omega_0) \right) \right] \right)$$
(3.16)

Here, r_j denotes the average distance between an individual proton j and the SPIONs in the cluster. C_Q is a scaling factor used to reduce computational time that accounts for the actual proton density in the voxel containing the SPION cluster by considering a total number of $3.342 \cdot 10^{29}$ protons/m³. These results will then be compared with the relaxation rate for regular NMR measurements at a similar concentration. Here, a relaxivity of $272 \text{ (mg/ml)}^{-1} \cdot \text{s}^{-1}$ was used, which was determined from the data of Figure C.1a, which will be discussed further in the next section.

3.2. Preparatory NMR measurements

To determine suitable SPION concentrations for ANMR measurements, preparatory NMR experiments were conducted to characterize T_1 and T_2 times of various aqueous SPION solutions. It is expected that the SPION concentrations influences two key aspects. On the one hand, increasing SPION concentration is expected to enhance modulation of the longitudinal relaxation rate due to an increased mean number of interacting spins, as described by Equation 2.23.

However, higher SPION concentrations also accelerate transverse relaxation, leading to shortened $T_2(^*)$ times. This rapid decay of transverse magnetization can greatly decrease the ability to detect any signal, thereby limiting the practical upper bound of usable SPION concentrations in ANMR experiments. Therefore, these preparatory measurements are essential to identify a concentration range that both allows potential enhancement of T_1 times and maintains a detectable signal.

For the work of this thesis, three types of SPION solutions from micromod Partikeltechnologie GmbH, Germany, were selected based on their coating, hydrodynamic diameter d_H , and correlation times, which are highlighted in Table 3.2. In this table, D refers to dextran, CLD to cross-linked dextran, and PEG to polyethylene glycol.

Table 3.2: Various SPION types used for this thesis from micromod Partikeltechnologie GmbH, Germany, with different surface coatings, hydrodynamic diameters d_H , and rotational and translational correlation times $\tau_{c,r}$ and $\tau_{c,t}$ in μ s calculated with Equation 2.11 and 2.12.

SPION type	Coating	d_H (nm)	$ au_{c,r}(\mu s)$	$ au_{c,t}(\mu s)$
synomag [®] -D	plain	50	11.1	49.8
nanomag®-D	PEG 300	130	195	875
nanomag®-CLD-redF	plain	300	$2.39 \cdot 10^{3}$	$10.8 \cdot 10^3$

These solutions were logarithmically diluted in pure water. Each measurement was performed 10 times, and the average relaxation time, including one standard deviation, was determined. For the T_1 and T_2 measurements, a saturation recovery (SR) sequence and a Carr-Purcell-Meiboom-Gill (CPMG) sequence were used, respectively. The results of the measurements are shown in Appendix C.

3.2.1. Measuring T_1

For the T_1 measurements, a saturation recovery (SR) sequence, as illustrated in Figure 3.2, was used. The longitudinal magnetization is initially saturated in this sequence using a $\pi/2$ RF pulse, similar to Figure 2.2. After each recovery time τ , a second $\pi/2$ RF pulse is applied to rotate the partially recovered longitudinal magnetization into the transverse plane. A π pulse is then played to minimize the influence of T_2 decay on the signal, after which the signal is read out from the FID. The measurement is then repeated multiple times with varying values for τ to sample the full recovery curve of the longitudinal magnetization. For simplicity, only the $\pi/2$ pulses and the FID are shown in Figure 3.2. Between the measurements, a relaxation delay of a duration of at least $5T_1$ is added to allow for full recovery of the longitudinal magnetization between sequences. The T_1 relaxation of the sample can then be determined by fitting the data points to Equation 3.17.

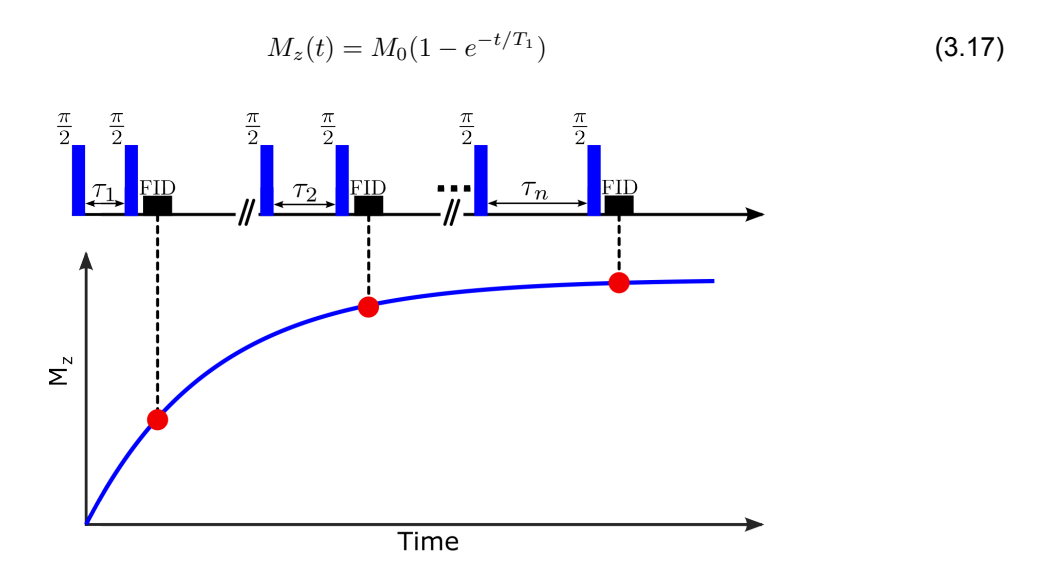


Figure 3.2: An illustration of the saturation recovery (SR) sequence used in this thesis to determine T_1 . A series of $\pi/2$ RF pulses is applied with varying values of τ , after which the signal can be read out from the FID. The data points can then be fitted with Equation 3.17 to determine T_1 .

3.2.2. Measuring T_2

In this thesis, the CPMG method is used to determine T_2 of the sample. As illustrated in Figure 3.3, the CPMG method consists of a single $\pi/2$ RF pulse at the start, followed by a train of π pulses [17]. The initial $\pi/2$ RF pulse tips the net magnetization into the transverse plane, resulting in dephasing due to spin interactions and field inhomogeneities. After a time $\tau=TE/2$, the first π pulse is applied to refocus the spins, resulting in a detectable echo after a time $TE=2\tau$. The series of π pulses mitigates dephasing caused by inhomogeneities, leading to a measurement of T_2 instead of T_2^* . The data points from the echo amplitudes can then be fitted using Equation 2.9 to determine T_2 .

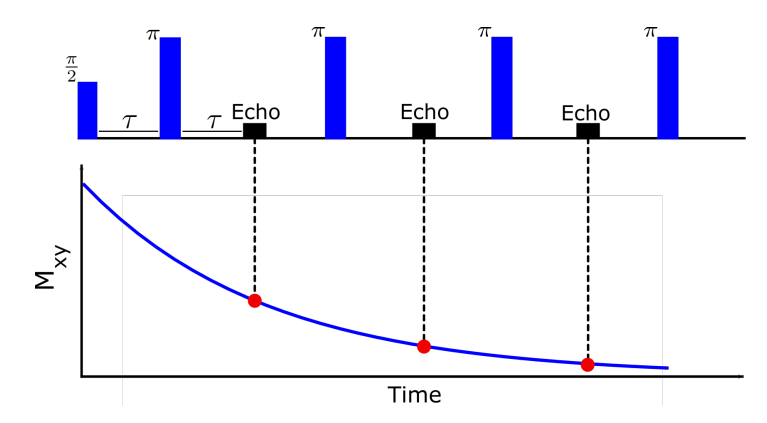


Figure 3.3: An illustration of the CPMG sequence used in this thesis to determine T_2 . First, a $\pi/2$ RF pulse is applied to tip the net magnetization vector into the transverse plane. This is followed by a train of π pulses to create an echo that can be detected after a time $\tau = TE/2$. The data points can then be fitted with Equation 2.9 to determine T_2 .

3.3. Acoustic NMR measurements

All of the (A)NMR measurements have been performed using an NMR time-domain analyzer from Resonance Systems GmbH, Germany, at a temperature of 35 °C and a field strength of 0.41 T corresponding to a Larmor frequency of 17.37 MHz. Before measurements, the resonance frequency and phase of the RF pulse generated by the NMR analyzer were calibrated.

3.3.1. SPION solutions

The effect of US on the T_1 relaxation times was investigated for all three SPION types. The concentrations and corresponding estimated T_1 relaxation times of the SPION solutions used in the ANMR experiments are provided in Table 3.3, as determined from Appendix C.

Table 3.3: SPION types used in the ANMR measurements, including their concentrations and estimated T_1 relaxation times with standard deviations.

SPION type	Concentration (mg/ml)	T_1 (ms)
synomag [®] -D	0.002	1300
nanomag [®] -D	0.003	1300
nanomag®-CLD-redF	0.02	1500

3.3.2. ANMR sequence

The sequence used for the ANMR measurements is shown in Figure 3.4. The conventional T_1 mapping sequence, described in section 3.2, was modified to enable interleaved acquisition of NMR and ANMR curves. To acquire an ANMR curve, an US pulse of duration τ_{US} is applied between the saturation pulse and the readout. The duration of the US pulse is chosen to be around 2 ms shorter than τ to avoid (electromagnetic) interference with the readout process, while still allowing the longest possible interaction period. For each saturation time, the measurement is repeated 10 times for synomag®-D and nanomag®-D, and 5 times for nanomag®-CLD-redF, while alternating between saturation periods with and without the US pulse. This interleaved approach minimizes signal drift due to confounding effects such as sedimentation between the NMR and ANMR measurements. Furthermore, the sample

was vortex-mixed between each set of repetitions to further minimize the impact of the confounding effects. The measured data is then fitted to Equation 3.17 to obtain T_1 .

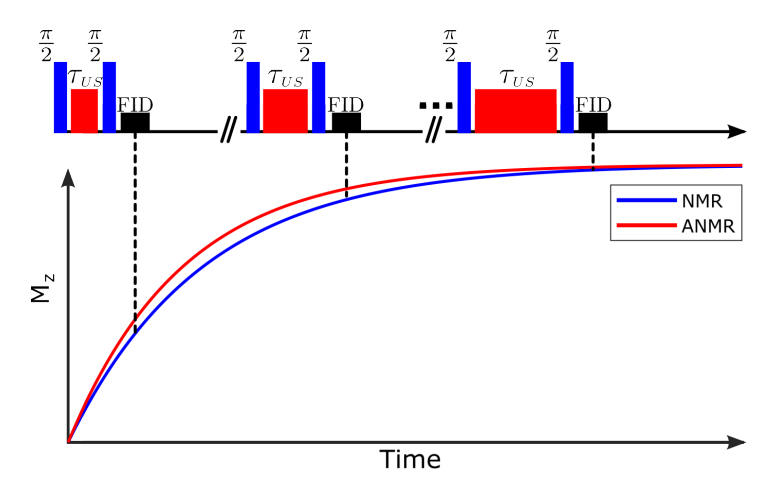


Figure 3.4: An illustration of the saturation recovery (SR) sequence used in this thesis to determine T_1 during ANMR measurements. The blue line shows a regular NMR measurement, where no US pulse is played. The red line shows an expected ANMR measurement. A series of $\pi/2$ RF pulses is applied with varying values US pulse durations (τ_{US}) after which the signal can be read out from the FID. The data points can then be fitted with Equation 3.17 to determine T_1 .

3.3.3. Experimental setup

A schematic overview of the experimental setup used for the ANMR measurements is shown in Figure 3.5. To allow for the ultrasound waves to be focused into the sample, a custom sample holder was designed. To that end, the vendor-provided glass vials were combined with a glass funnel to allow focusing of the US wave into the sample and closed off with an acoustically absorbing layer to prevent reflection of the US wave. The isocenter of the magnetic field is in the middle of the NMR coils at a depth of approximately 10.3 cm. The ultrasound transducer generates focused waves with a focal depth of 9.65 cm, meaning that the focus is 0.65 cm before the isocenter of the NMR analyzer. During the measurements, the time-domain analyzer triggers the first arbitrary function generator (AFG). A second AFG is triggered, which then sends the US signal to the amplifier with an effective gain of 31 dB, after which the signal is amplified to an acoustic pressure of choice. The generated US wave and trigger are monitored using an oscilloscope. The voltage generated at 17.37 MHz was estimated to be approximately 40 Vpp, based on a visual inspection of the peak-to-peak amplitude displayed on the oscilloscope. The NMR time-domain analyzer is coded such that it triggers the ultrasound generator to generate an US wave with a frequency that exactly matches the frequency of the NMR analyzer. In Figure 3.6, a photograph of the experimental setup is shown.

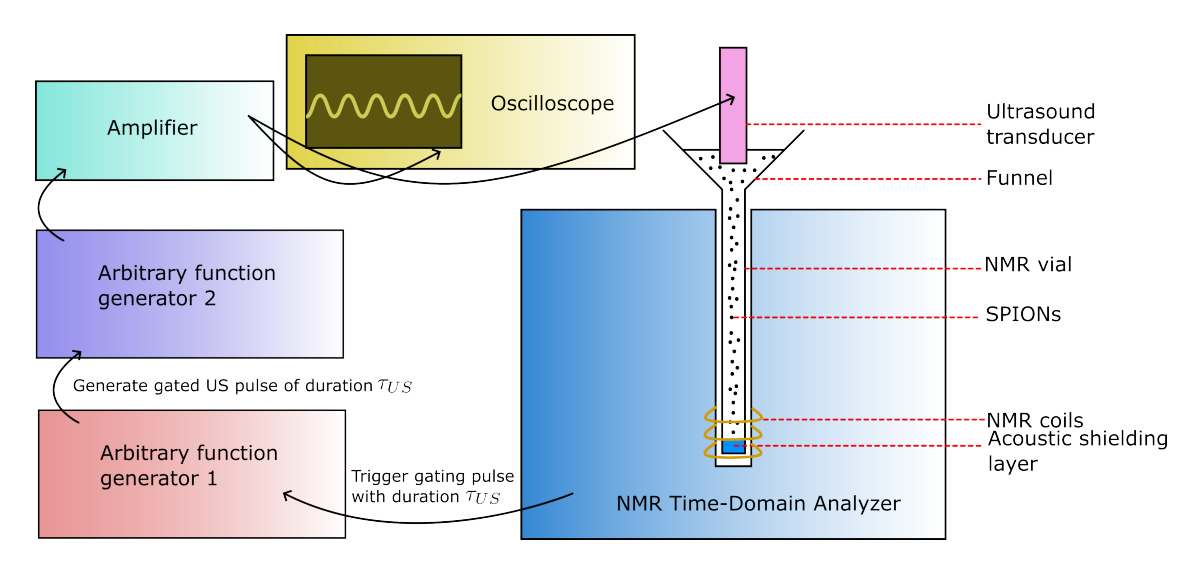


Figure 3.5: Schematic of the experimental setup for ANMR measurements. The NMR time-domain analyzer triggers the arbitrary function generator (AFG) 1, which triggers AFG 2, which generates a signal at the Larmor frequency. This signal is amplified and sent to an ultrasound transducer, which generates focused acoustic waves directed into an NMR vial with a funnel containing SPION solutions. The focal depth of the transducer is 9.65 cm, and the isocenter of the magnetic field is inside the NMR coils at 10.3 cm. An oscilloscope monitors the ultrasound waveform.

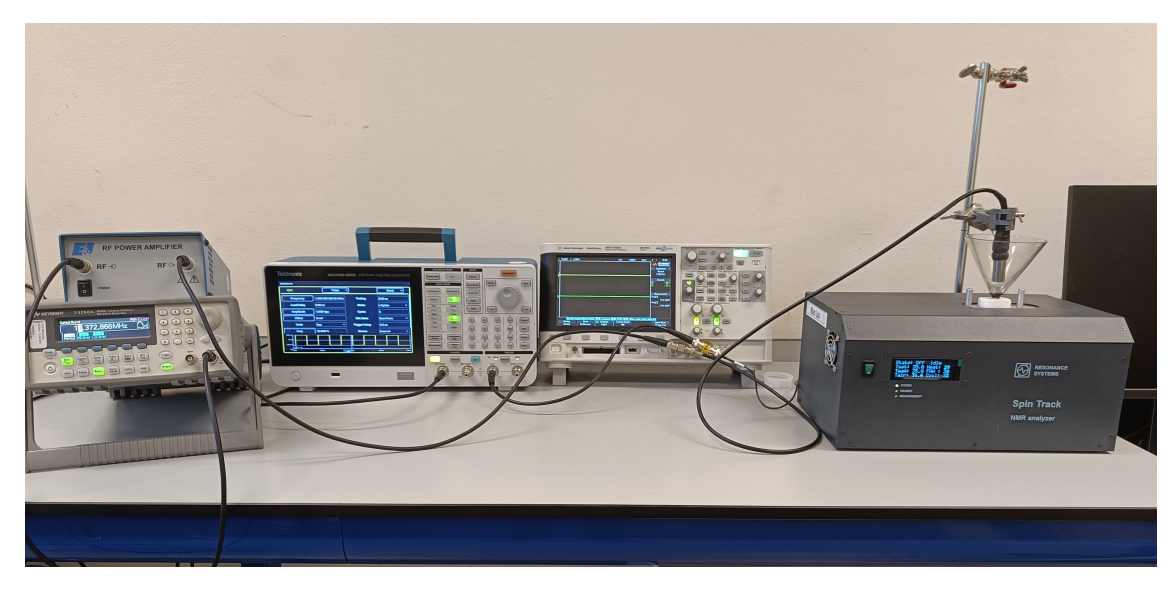


Figure 3.6: A photograph of the experimental setup used for the ANMR measurements.

4

Results

In analogy to chapter 3, the following Results chapter will be divided into two parts. First, the results of the US-modulated SPION relaxation model are presented. Second, the results of the experimental ANMR measurements are provided.

4.1. Ultrasound-modulated SPION relaxation model

The simulated acoustic pressure field for an US frequency of f=20 MHz and a peak acoustic pressure of 1 MPa is illustrated in Figure 4.1, with the position of the SPION cluster at (0.32 mm, -0.03 mm) indicated in red. Due to wave interference, the pressure exceeds 1 MPa at the center of the focus, but attenuates rapidly beyond the focal region. SPION clusters located farther from the focus are primarily exposed to a field similar to a plane wave, resulting in forces directed along the wave propagation axis. In contrast, clusters at the focal point experience additional orthogonal force components, leading to a greater net torque.

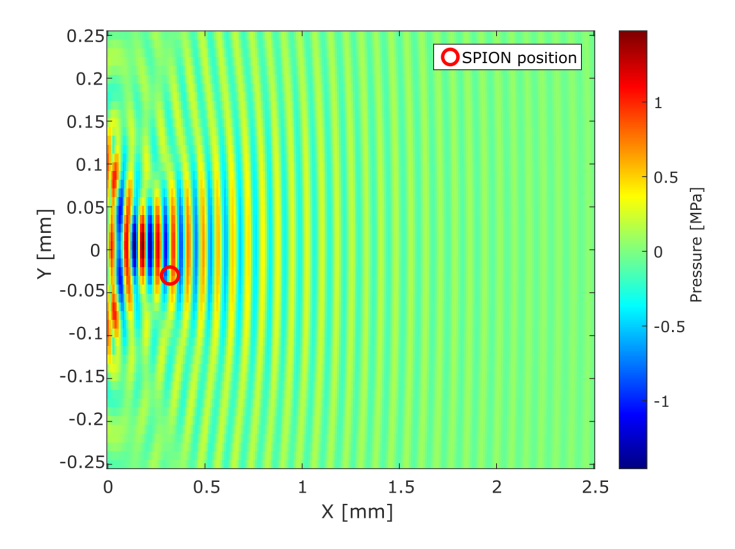


Figure 4.1: A simulated acoustic pressure field over an area of 2.5 mm by 0.5 mm using the k-Wave MATLAB toolbox for a focused transducer with a focal depth of 0.25 mm, an US frequency of 20 MHz, and an acoustic pressure of 1 MPa. The red circle indicates the position (0.32 mm, -0.03 mm) of the SPION. The highest pressure occurs at the focal point as a result of wave interference, with a reduction in pressure beyond the focus due to attenuation.

4.1.1. SPION dynamics

For a cluster of N=12 SPIONs as shown in Figure 3.1, the translational and rotational dynamics are modeled as described in section 3.1 for a time period of 3.5 μ s. The resulting simulated rotational and

translational dynamics are shown in Figure 4.2 and 4.3, respectively. For an US wave incident from the left, a maximum angular displacement of $2\theta\approx 6.5\cdot 10^{-3}$ degrees, and a maximum translational displacement of around 5 nm is observed. From Figure 4.3, it can also be noted that the motion of the SPION cluster is closely correlated with the motion of the water (shown in black). This behaviour is highlighted in Figure 4.3a, where lagging motion of the SPIONs due to the high density and large size with respect to the medium is observable. In Figure 4.3b, the relative displacement between the SPION cluster and the water particles is presented. This figure indicates that the maximum relative displacement between the medium and the SPIONs is around 0.45 nm.

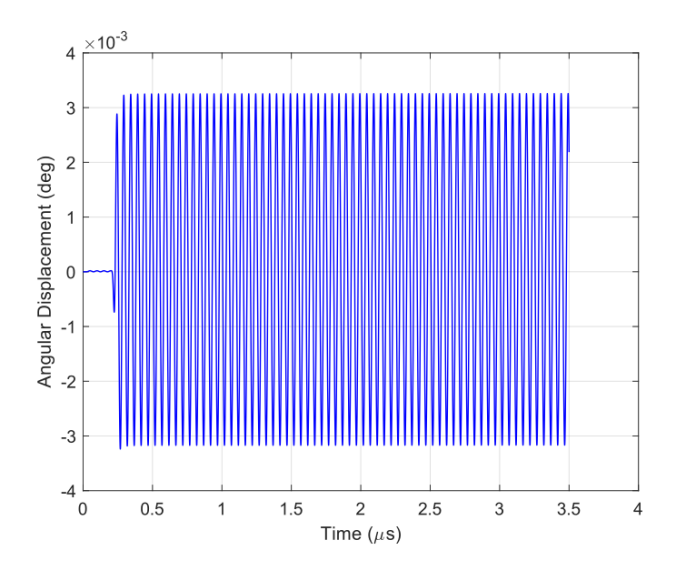


Figure 4.2: The simulated angular displacement (in degrees) of the SPION cluster in water from Figure 3.1 for an US frequency of 20 MHz and an acoustic pressure of 1 MPa over a time period of 3.5 μ s. A maximum angle of $2\theta \approx 6.5 \cdot 10^{-3}$ degrees is observed.

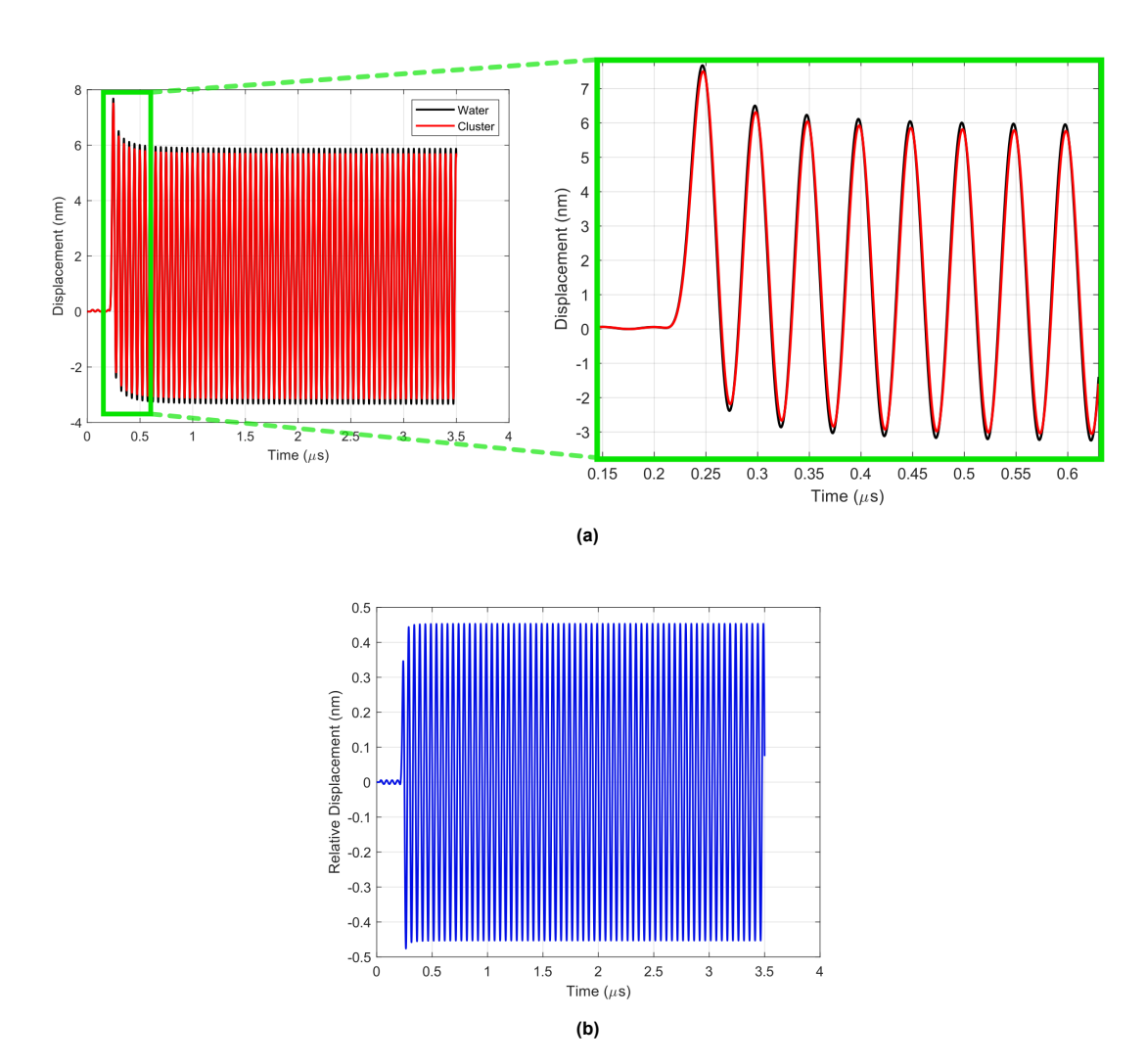


Figure 4.3: (a) Left: The simulated displacement (in nm) of the SPION cluster from Figure 3.1 for an US frequency of 20 MHz and an acoustic pressure of 1 MPa over a time period of 3.5 μs. Here, the SPION cluster displacement is in red, and the water proton displacement is in black. Right: A zoomed-in portion of Figure (a) highlighted in the green rectangle. Due to the larger density and size of the cluster compared to water protons, the SPION cluster experiences less displacement, which is temporally lagging with respect to the displacement of the water protons. (c) The relative displacement in nm between the water protons and the SPION cluster.

The simulated interaction of US waves with increasing cluster sizes results in an exponential decay of both rotational and translational displacement (Figure 4.4). A minimal rotational displacement of $6.25 \cdot 10^{-3}$ degrees is observable for the largest clusters containing 100 SPIONs (Figure 4.4a), corresponding to a diameter of around 575 nm (Figure 4.4b). For a cluster of approximately 75 nm, a rotation of $6.6 \cdot 10^{-3}$ degrees is expected. The maximum relative translational displacement, referring to the maximum distance between the SPION cluster and water molecules, exhibits a minimum of around 0.1 nm for the smallest cluster and a maximum of approximately 1.1 nm for the largest cluster (Figure 4.4c and 4.4d). It is to be noted that the translational displacement of a cluster only depends on the number of SPIONs, not on the spatial arrangement. Therefore, error bars are omitted in the corresponding figures.

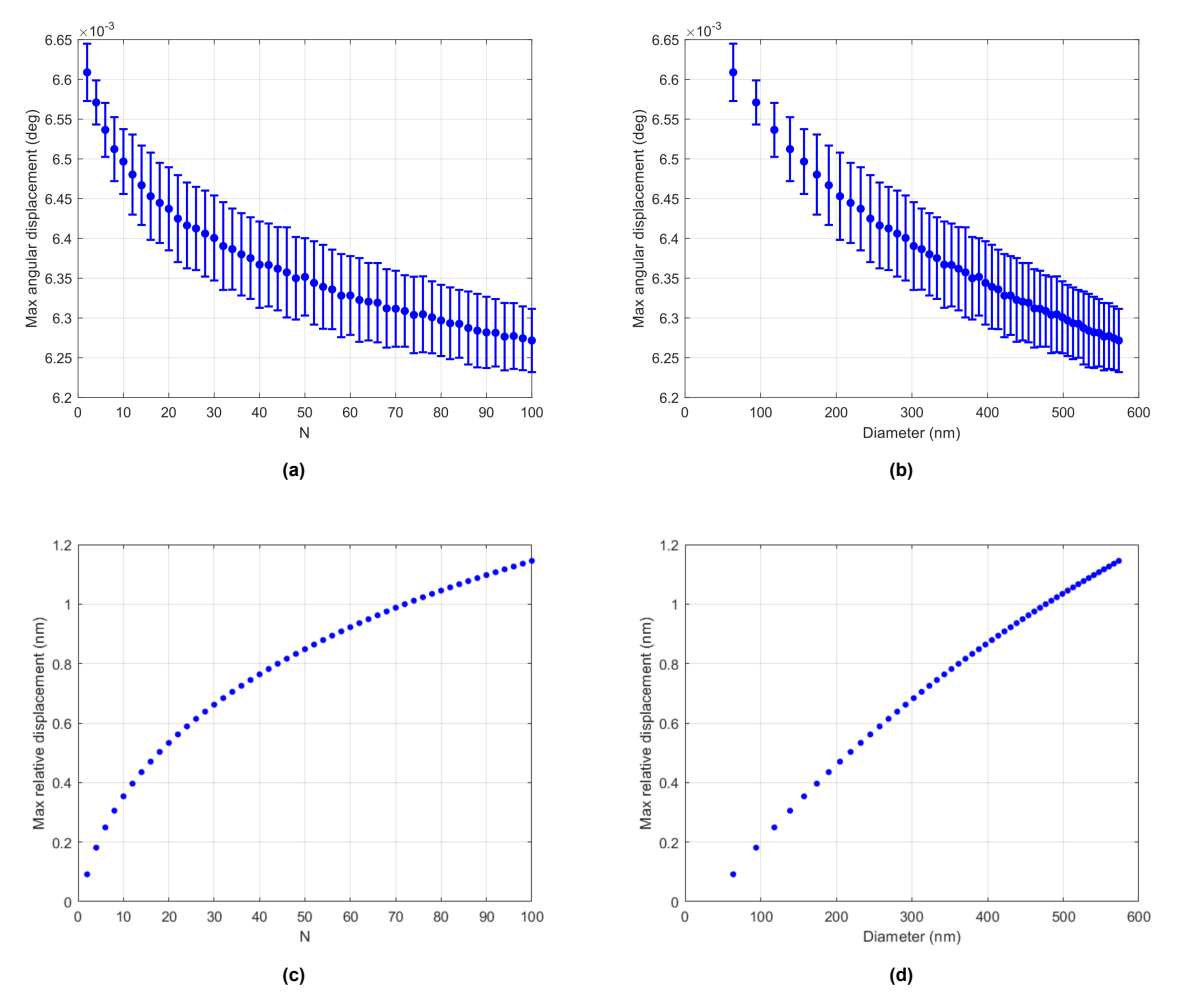


Figure 4.4: Simulations of rotational and translational dynamics of SPION clusters in a 20 MHz, 1 MPa acoustic pressure field. (a, b) Average maximum angular displacement (°) with standard deviation bars, plotted against (a) the number of SPIONs per cluster N, and (b) cluster diameter (from Equation 3.10). The largest rotational motion occurs for the smalles cluster. (c, d) Average maximum relative displacement between SPION clusters and water (nm), plotted against (c) N, and (d) cluster diameter. The largest relative translational distance is exhibited by the largest SPION cluster. Each cluster size was simulated 1000 times. As translational displacement is determined by the summation of the acoustic forces over the entire cluster (Equation 3.8), clusters with the same number of SPIONs experience the exact same displacement. Therefore no error bars are shown in (c) and (d).

4.1.2. Local magnetic field fluctuations and its influence on R_1

The simulated fluctuations in the local magnetic field for a cluster of N=5 SPIONs experienced by a proton located 100 nm from the cluster's center yield an oscillatory magnitude around 0.598 mT, as shown in Figure 4.5a. A gradual increase in mean B value is notable. Its corresponding spectral density is shown in Figure 4.5b. For comparison, the spectral density simulated based on a Nuclear Magnetic Relaxation Dispersion (NMRD) profile for SPIONs, where relaxation due to Brownian motion is dominant [24], is shown in Figure 4.5c. The spectral density from Figure 4.5b decreases as a function of the driving frequency and exhibits a peak at f=20 MHz. The NMRD profile shows a similar reduction in spectral density, but a distinct peak is not observable.

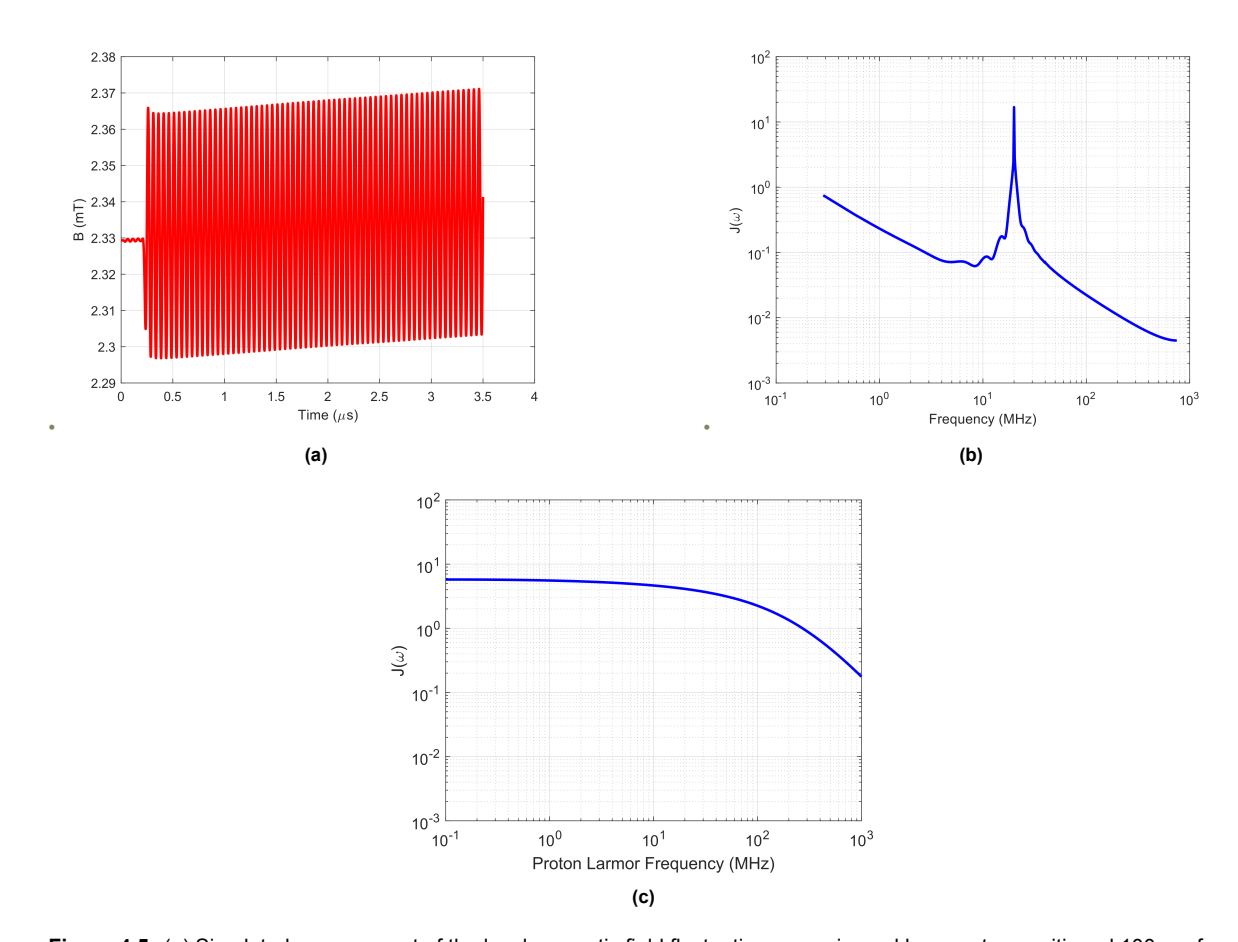


Figure 4.5: (a) Simulated x-component of the local magnetic field fluctuations experienced by a proton positioned 100 nm from the cluster's center of mass, showing oscillatory behaviour. (b) Corresponding spectral density in the entire voxel, exhibiting a distinct peak at the 20 MHz driving frequency. (c) For comparison, the spectral density of a Nuclear Magnetic Relaxation Dispersion (NMRD) profile [24] for a spherical SPION with $R_g=53.8$ nm corresponding to a cluster size of N=5 is shown.

The calculated relaxation rate assignable to the US waves at the concentration corresponding to the SPION cluster in the voxel is $R_{1,US} = 3.08 \cdot 10^3 \text{ s}^{-1}$. The ratio of $R_{1,US}$ to the relaxation rate in regular NMR R_1 changes as a function of concentration, with the highest effect of approximately 33% expected at the largest concentration (Figure 4.6).

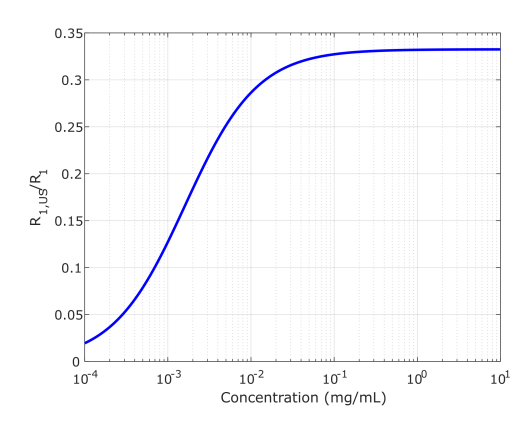


Figure 4.6: The simulated ratio of the longitudinal relaxation rate induced by US $(R_{1,US})$ to the relaxation rate R_1 for an increasing SPION concentration in mg/ml. A maximum relaxation rate modulation of around 33% is observed.

4.2. Acoustic NMR measurements

To investigate the influence of ultrasound on longitudinal relaxation rates, NMR and ANMR measurements of the T_1 relaxation time were conducted across a range of recovery times. These measurements were performed on three types of aqueous SPION solutions with particle sizes of 50, 130, and 300 nm, as described in Table 3.3. The resulting averaged signal amplitudes, including one standard deviation, and corresponding magnetization recovery fits are presented in Figure 4.7. All T_1 and R_1 values for NMR and ANMR measurements are listed in Table 4.1. For all three SPION solutions, no significant modulation of relaxation rates is observed.

Table 4.1: T_1 and R_1 including one standard deviation of NMR and ANMR measurements on three SPION solutions of concentrations that were expected to yield similar T_1 .

SPION type	Concentration (mg/ml)	NMR		ANMR	
		$T_1 \pm std$ (ms)	$R_1 \pm std$ (s ⁻¹)	$T_1 \pm std$ (ms)	$R_1 \pm std$ (s ⁻¹)
synomag [®] -D	0.002	1120 ± 27.6	0.893 ± 0.024	1120 ± 27.5	0.894 ± 0.024
nanomag [®] -D	0.003	1190 ± 22.2	0.840 ± 0.014	1200 ± 23.9	0.836 ± 0.017
nanomag®-CLD-redF	0.02	1960 ± 69.6	0.510 ± 0.020	1950 ± 78.4	0.513 ± 0.021

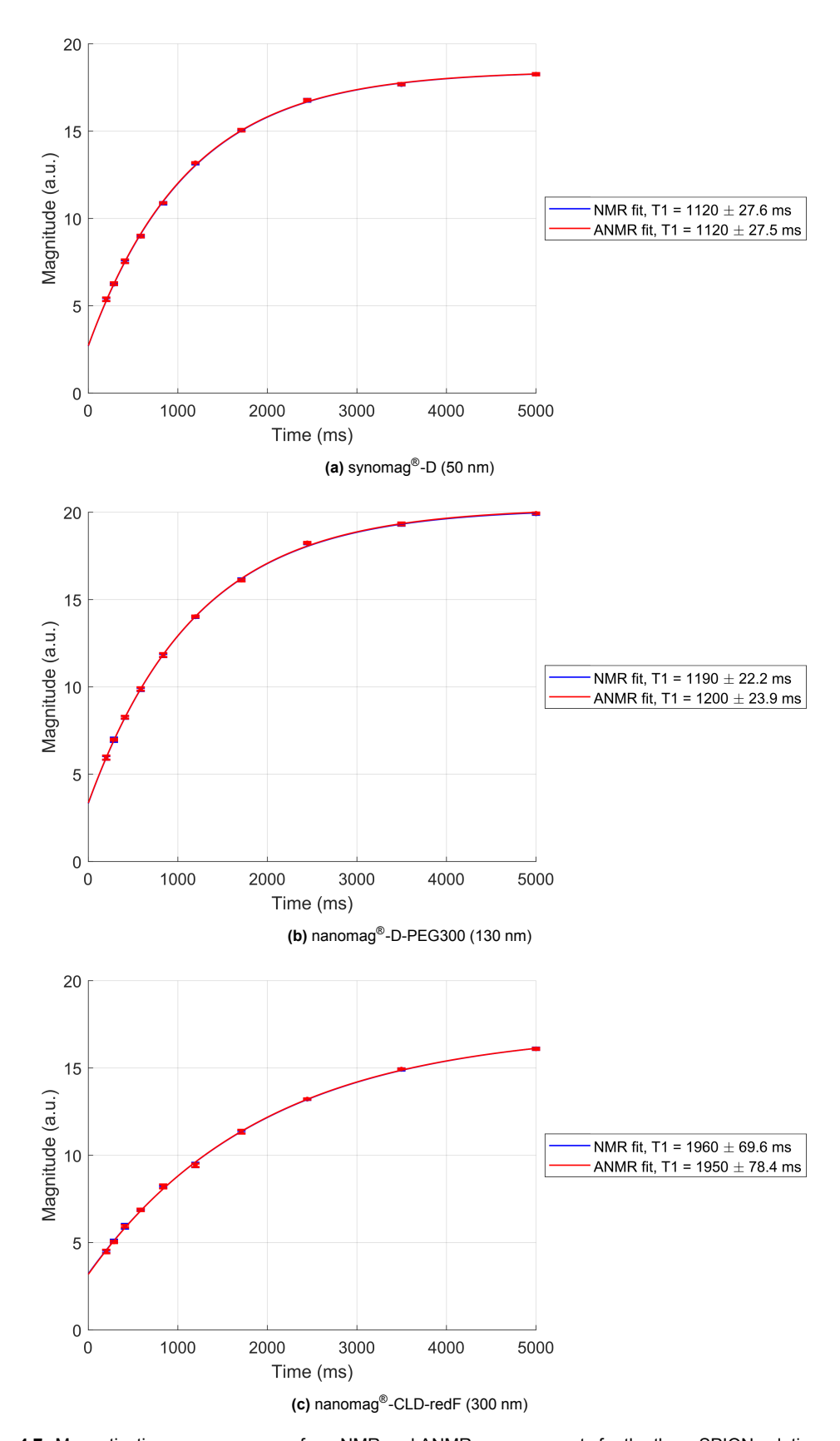


Figure 4.7: Magnetization recovery curves from NMR and ANMR measurements for the three SPION solutions: (a) synomag $^{\otimes}$ -D (50 nm), (b) nanomag $^{\otimes}$ -D-PEG300 (130 nm), and (c) nanomag $^{\otimes}$ -CLD-redF (300 nm). Data points represent averaged signal amplitudes with error bars indicating one standard deviation. Solid lines correspond to exponential fits used to estimate the longitudinal relaxation time T_1 . No significant difference in T_1 was observed between NMR and ANMR measurements for any of the samples.

5

Discussion

This study explored the potential of US-induced modulation of T_1 relaxation rates in aqueous solutions containing SPIONs. The focus of this research was twofold. First, a theoretical description was developed to model SPION dynamics and the resulting local magnetic field fluctuations induced by US waves. Second, US-induced modulation of longitudinal relaxation rates was experimentally investigated with ANMR measurements. Simulation experiments demonstrated that translational motion contributes more significantly to US-modulated longitudinal relaxation rates than rotational motion. Furthermore, a distinct peak of the spectral density at the Larmor frequency was exhibited in the simulation when US was applied. However, experimental ANMR measurements showed no significant change in relaxation rates. The findings and future research directions of the model simulations and ANMR measurements will be discussed in two separate sections.

5.1. Ultrasound-modulated SPION relaxation model

The model proposed in this thesis has served as a valuable tool in the determination of short-term dynamics of SPION clusters. Unlike many other models, where the acoustic force is averaged over one period to compute the net translational displacement of a particle [43, 44, 45], this model simulates both rotational and translational motion as a function of the instantaneous acoustic force. These dynamics are then used to compute the local magnetic field fluctuations to determine the change in relaxation rate assignable to the US waves. By directly coupling SPION cluster motion to relaxation behaviour, this model provides an understanding of the individual contribution of rotational and translational motion to relaxation mechanisms.

5.1.1. Interpretation of results

In the study by Vuong et al. [11], translational motion is considered the dominant contributor to dipole-dipole interaction modulation in ANMR, as US waves are expected to primarily influence the translational displacement of particles. In contrast, other research proposes that rotational motion plays a more significant role in the US-induced modulation of relaxation rates [13, 14]. Consistent with a similar model, previously published [13], the maximum predicted angular rotation for a SPION cluster is around $2\theta \approx 6.6 \cdot 10^{-3}$ degrees. This corresponds to a translation of around 0.1-1 nm for the outermost SPION in a cluster, which suggests a much lower contribution of rotational motion compared with translational motion, which is about 8-9 nm. These results suggest that translational motion effects are indeed the main contributor to longitudinal relaxation rates and that the presence of asymmetry is likely less relevant for the effectiveness of US modulation.

It should be noted that the radius of gyration decreases with a square root factor proportional to the number of SPIONs in the cluster. This implies that clusters containing few SPIONs tend to be more asymmetric in shape than large clusters. However, the difference in angular rotation between the smallest and largest clusters is approximately only $0.35 \cdot 10^{-3}$ degrees, suggesting that the influence of asymmetry in SPION clusters on the rotational motion is minimal. This further contributes to the indication that asymmetry in SPION clusters is not a necessary condition for effective modulation of

relaxation rates.

The simulation results show a clear trend between SPION cluster size and the maximum relative displacement between the cluster and surrounding water molecules. As this relative displacement increases, the cluster becomes more stationary with respect to the surrounding fluid, allowing more water protons to move past the SPION-induced magnetic field gradients. This is expected to lead to an increased number of dipolar interactions and, consequently, an enhanced longitudinal relaxation rate. This corresponds with the theoretical framework proposed by Vuong et al. [11], where larger SPIONs are expected to enhance longitudinal relaxation rates more than small SPIONs.

Comparing the resulting spectral density with the spectral density of the NMRD profile, the main difference lies in the peak exhibited by the US modulated spectral density function at 20 MHz. This peak is not observed in the spectral density of the NMRD profile, as only Brownian motion is considered here. The low-frequency component of the ANMR spectral density between 10^{-1} and 10^{0} originates from the time instant at which the US wave has not yet reached the SPION cluster. A combination of both models would result in a more accurate spectral density shape for the determination of the longitudinal relaxation rate, as both Brownian motion and motion due to US waves will be accounted for.

Considering the ratio $R_{1,US}/R_1$, a minimal effect of 2.5% is observed at a concentration of 10^{-4} mg/ml. This ratio increases with higher concentrations, reaching a maximum of about 33% at 10^{-1} mg/ml. Beyond this concentration, the effect of US waves on the change in R_1 appears to plateau. This plateau might suggest that the system has reached saturation, where additional dipolar interactions between protons and SPIONs are no longer possible.

5.1.2. Model assumptions and recommendations for future research

It should be noted that the model is based on several assumptions to allow both physical accuracy and to reduce complexity. Firstly, it is assumed that SPION clusters will behave as rigid bodies during translation and rotation. As a result, the individual SPIONs within a cluster are not expected to be displaced relative to one another due to the acoustic pressure. This is a reasonable assumption for small clusters of SPIONs with similar shapes and sizes. For larger clusters that experience an inhomogeneous acoustic pressure field, this assumption would not hold. However, due to the very short simulated sound period of 50 ns and because $\lambda \gg R_g$ for the SPIONs used in this thesis, the internal dynamics of SPION clusters were considered negligible. This implies that all forces act uniformly on the cluster as a whole, justifying the rigid-body approximation. This introduces a second key assumption: the cluster size is assumed to be much smaller than the acoustic wavelength. For example, in water, the wavelength at 20 MHz is 75 μ m, which is over 100 times larger than the size of a SPION cluster with N=100, making this approximation well-justified.

Another assumption worth mentioning is that interactions between individual SPIONs within a cluster are ignored. For SPIONs, the main attractive forces are van der Waals forces and magnetic forces, while repulsive contributions arise primarily from electrostatic forces and repulsive forces. To improve the physical accuracy of the model, the Derjaguin-Landau-Verwey-Overbeek theory [46, 47], which combines van der Waals and electrostatic forces, could be incorporated. This would allow modeling the effect of acoustic forces on SPION aggregate formation or destruction, which could influence a change in relaxation rate [24].

Moreover, as the primary aim of the model was to analyze rotational and translational motion, Brownian motion was ignored. In a one-dimensional scenario, the diffusion length L of a particle can be determined by $L=\sqrt{2D_tt}$, with D_t being the diffusion coefficient and t being the characteristic time of the motion, with t equal to the period of the sound wave [48]. Following this equation, water molecules exhibit a diffusion length that is approximately 10 times greater than that of SPIONs, resulting in less efficient dipolar interactions. This significantly affects the magnitude of the ANMR spectral density peak and, consequently, the relaxation rates. To incorporate Brownian motion in the model, the equations of motion can be reconsidered by implementing an additional term representing Brownian noise [49].

5.2. Acoustic NMR measurements

To summarize the hypothesis, the presence of SPIONs may enable the modulation of longitudinal relaxation times in water by acoustic waves. Due to the strong coupling between US and thermal motion

effects, larger SPIONs are predicted to exhibit greater modulation of relaxation rates than smaller ones. However, experimental ANMR results did not reveal a significant reduction in \mathcal{T}_1 times for any of the three SPION types.

One possible explanation for the absence of R_1 modulation is that the mechanical oscillations induced by US were too weak to induce sufficient magnetic field fluctuations at the Larmor frequency. This could potentially stem from the acoustic pressure being too low, which may have resulted from the fact that the transducer focal point was not at the same depth as the isocenter of the NMR analyzer. Additionally, the transducer aperture was larger than the diameter of the vial, meaning that not all acoustic energy was focused. This problem was partially solved with the funnel attached to the top of the vial, but it might still have resulted in decreased acoustic pressures.

The model predicts that both rotational and translational displacements are proportional to the pressure of the acoustic wave, meaning that larger pressures lead to enhanced modulation of R_1 . Furthermore, at sufficiently high acoustic pressures, the oscillatory motion induced by US waves would dominate over Brownian motion effects, enhancing relaxation rate modulation. However, in the current experimental setup, the acoustic pressure could be insufficient to achieve this, allowing Brownian motion to remain the dominant influence. This warrants direct assessment of the acoustic pressure within the sample to more accurately assess the US-induced modulation.

During ANMR measurements, a gradual increase in T_1 and T_2 was observed. Especially for high concentrations, a strong decrease in signal was notable. As mentioned in section 3.2, the signal of the T_1 measurements is assumed to be independent of T_2 decay. However, if the echo time TE is not chosen to be much smaller than T_2 , the signal is influenced by T_2 decay, especially when T_2 increases over time. Based on this dependence, an increase in T_1 and T_2 of the solutions over time poses significant issues when attempting to measure steady signals.

Three possible scenarios influencing the change in signal were considered: sedimentation, aggregation, and adhesion of SPIONs to the glass surface of the vials. As sedimentation rates are known to scale with the squared particle radius r^2 [50], the terminal velocity of SPIONs due to sedimentation can be considered to be negligible throughout the ANMR measurements conducted in this thesis. Nevertheless, to prevent sedimentation during the acquisition, samples were vortex-mixed in between individual measurements to suppress short-term sedimentation. Furthermore, sedimentation would result in an increased SPION concentration at the bottom of the vial, where the isocenter and receive/transmit coils of the NMR system are located. Under the experimental conditions with sufficiently short TE minimizing the effects of T_2 shortening on the signal, this increased local concentration would be expected to reduce T_1 and thus increase the signal. However, a decrease in signal was observed, further indicating that sedimentation is unlikely to be the primary cause of lengthened T_1 and T_2 .

To determine the effect of aggregation on transverse relaxation rates R_2 , it should be noted that SPION concentration plays a significant role in determining the relaxation behaviour. If aggregates are formed, the effective number of independent SPION particles decreases [24], leading to a reduced effective concentration. This reduction aligns with the observed increase in T_2 . Furthermore, as R_1 is proportional to the concentration and inversely proportional to the SPION radius [24], aggregation would also cause a decrease in R_1 , consistent with the observed experimental results. These observations collectively suggest that SPION aggregation likely occurs during (A)NMR measurements. Given the indications of aggregation from relaxation measurements, future studies can benefit from Transmission Electron Microscopy to directly visualize and confirm the formation of SPION aggregates.

Throughout the ANMR measurements, it was observed that the synomag®-D and nanomag®-CLD-redF solutions showed clear dark brown spots on the sides of the vial when exposed to the external magnetic field for a long period. This indicated a strong adhesion of SPIONs to the glass surface, resulting in a loss of effective concentration and an increase in measured T_1 . However, this was not observed for the nanomag®-D-PEG300 solution. This is likely a result of the different coatings of the three SPION types. Synomag®-D and nanomag®-CLD-redF are only coated in dextran, a polar molecule [51], which increases the SPIONs' affinity for glass surfaces. The nanomag®-D-PEG300, however, is additionally coated in PEG, which, as a large polymer, decreases the adhesion to glass. This highlights the importance of surface-coated SPIONs to allow stable relaxation rates.

6

Conclusion

This thesis investigated the modulation of longitudinal relaxation rates in NMR of aqueous solutions containing SPIONs using resonant US waves. First, a theoretical model on SPION cluster dynamics in an US field and its influence on local magnetic field fluctuations was developed and evaluated. Second, experimental ANMR measurements on three SPION solutions with particle diameters of 50, 130, and 300 nm were conducted to investigate the effect of particle size on US-induced relaxation rate modulation.

Simulation experiments demonstrated that translational motion contributes more significantly to US-modulated longitudinal relaxation rates than rotational motion. The modeled spectral density confirms a significant increase at the US driving frequency, which was not present in the NMRD profile. This suggests resonant magnetic field fluctuations with the Larmor frequency were exhibited by the SPION clusters. These results support the hypothesis that US can modulate longitudinal relaxation rates in aqueous SPION suspensions.

However, experimental ANMR measurements on three SPION solutions with particle diameters of 50, 130, and 300 nm showed no significant modulation of relaxation rates. Potential reasons include insufficient acoustic pressure to induce magnetic field fluctuations at the Larmor frequency, thereby failing to dominate over Brownian motion. In addition, experimental limitations such as SPION aggregation and adhesion to glass surfaces reduced signal stability and effective SPION concentration.

Despite the negative experimental results, this work provides important insights into the underlying relaxation mechanisms of SPION solutions for both NMR and ANMR. Future work should aim to improve the model's physical accuracy by implementing Brownian motion into the equations of motion. Furthermore, acoustic pressure levels should be measured and, if possible, increased. Lastly, to improve signal stability, conducting ANMR measurements on SPIONs with surface coatings aimed at minimizing aggregation and adhesion to glass is recommended. If effective ultrasound-induced modulation in SPION solutions can be reliably achieved, ANMR may offer a promising basis for enabling localized contrast enhancements in low-field MRI.

- [1] I. I. Rabi et al. "A New Method of Measuring Nuclear Magnetic Moment". In: *Physical Review* 53.4 (Feb. 1938), p. 318. DOI: 10.1103/physrev.53.318. URL: https://doi.org/10.1103/physrev.53.318.
- [2] Juergen Hennig. "An evolution of low-field strength MRI". In: *Magnetic Resonance Materials in Physics Biology and Medicine* 36.3 (June 2023), pp. 335–346. DOI: 10.1007/s10334-023-01104-z. URL: https://doi.org/10.1007/s10334-023-01104-z.
- [3] Anatole Abragam. Principles of Nuclear Magnetism. Jan. 1993.
- [4] Dan I. Bolef and Ronald K. Sundfors. *Nuclear Acoustic resonance*. Jan. 1993. DOI: 10.1016/b978-0-12-111250-9.x5001-4. URL: https://doi.org/10.1016/b978-0-12-111250-9.x5001-4.
- [5] A. Kastler. "Quelques réflexions à propos des phénomènes de résonance magnétique dans le domaine des radiofréquences". In: Experientia 8.1 (Jan. 1952), pp. 1–9. DOI: 10.1007/bf02168 877. URL: https://doi.org/10.1007/bf02168877.
- [6] S. A. Al'Tshuler. "Resonance Absorption of Ultrasound in Paramagnetic Salts". In: SOVIET PHYSICS-JETP 1.1 (July 1955), p. 29.
- [7] W. G. Proctor and W. H. Tanttila. "Influence of Ultrasonic Energy on the Relaxation of Chlorine Nuclei in Sodium Chlorate". In: *Physical Review* 101.6 (Mar. 1956), pp. 1757–1763. DOI: 10.1103/physrev.101.1757. URL: https://doi.org/10.1103/physrev.101.1757.
- [8] L O Bowen. "Nuclear magnetic acoustic resonance and Debye vibration potentials in non-viscous liquids". In: *Proceedings of the Physical Society* 87.3 (Mar. 1966), pp. 717–720. DOI: 10.1088/0370-1328/87/3/312. URL: https://doi.org/10.1088/0370-1328/87/3/312.
- [9] A.V. Alekseev and U.Kh. Kopvillem. "Pseudospin quantum acoustics in liquids". In: *Ultrasonics* 18.2 (Mar. 1980), pp. 76–80. DOI: 10.1016/0041-624x(80)90140-7. URL: https://doi.org/10.1016/0041-624x(80)90140-7.
- [10] Guillaume Madelin et al. *NMR Characterization of Mechanical Waves*. Jan. 2004, pp. 203–244. DOI: 10.1016/s0066-4103(04)53004-1. URL: https://doi.org/10.1016/s0066-4103(04)53004-1.
- [11] Quoc Lam Vuong, Yves Gossuin, and Pierre Gillis. "Acoustical enhancement of nuclear magnetic relaxation rates in liquids". In: *Physical Review B* 77.21 (June 2008). DOI: 10.1103/physrevb. 77.212404. URL: https://doi.org/10.1103/physrevb.77.212404.
- [12] J. Mende et al. "Nuclear acoustic resonance in fluids using piezoelectric nanoparticles". In: *Journal of Magnetic Resonance* 203.2 (Dec. 2009), pp. 203–207. DOI: 10.1016/j.jmr.2009.12.019. URL: https://doi.org/10.1016/j.jmr.2009.12.019.
- [13] Nouri Mokhtar Elmiladi. "Proton Spin-Lattice Relaxation in Colloidal Aqueous Solutions with Resonant Ultrasound". PhD thesis. Rheinische Friedrich-Wilhelms-Universität Bonn, Aug. 2010. URL: https://hdl.handle.net/20.500.11811/4639.
- [14] Christian Joachim Höhl. "Wechselwirkung zwischen Ultraschall & Proton-Spin in wässriger Lösung". PhD thesis. Rheinische Friedrich-Wilhelms-Universität Bonn, Mar. 2011. URL: https://hdl.handle.net/20.500.11811/4937.
- [15] None Wahajuddin and None Arora. "Superparamagnetic iron oxide nanoparticles: magnetic nanoplat-forms as drug carriers". In: *International Journal of Nanomedicine* (July 2012), p. 3445. DOI: 10.2147/ijn.s30320. URL: https://doi.org/10.2147/ijn.s30320.
- [16] P. Zeeman. "The Effect of Magnetisation on the Nature of Light Emitted by a Substance". In: Nature 55.1424 (Feb. 1897), p. 347. DOI: 10.1038/055347a0. URL: https://doi.org/10.1038/055347a0.

[17] Robert W. Brown et al. *Magnetic Resonance Imaging: Physical Principles and Sequence Design*. June 1999. URL: http://leseprobe.buch.de/images-adb/5b/28/5b28d2ff-ced6-4acb-baf6-1039e9c81743.pdf.

- [18] Joao Tourais, Chiara Coletti, and Sebastian Weingärtner. *Brief Introduction to MRI Physics*. Jan. 2022, pp. 3–36. DOI: 10.1016/b978-0-12-822726-8.00010-5. URL: https://doi.org/10.1016/b978-0-12-822726-8.00010-5.
- [19] F. Bloch. "Nuclear induction". In: *Physical Review* 70.7-8 (Oct. 1946), pp. 460–474. DOI: 10. 1103/physrev.70.460. URL: https://doi.org/10.1103/physrev.70.460.
- [20] David J. Craik, Anil Kumar, and George C. Levy. "MOLDYN: a generalized program for the evaluation of molecular dynamics models using nuclear magnetic resonance spin-relaxation data". In: *Journal of Chemical Information and Computer Sciences* 23.1 (Feb. 1983), pp. 30–38. DOI: 10.1021/ci00037a006. URL: https://doi.org/10.1021/ci00037a006.
- [21] N. Bloembergen, E. M. Purcell, and R. V. Pound. "Relaxation effects in nuclear magnetic resonance absorption". In: *Physical Review* 73.7 (Apr. 1948), pp. 679–712. DOI: 10.1103/physrev. 73.679. URL: https://doi.org/10.1103/physrev.73.679.
- [22] Shenggen Yao et al. "NMR measurement of biomolecular translational and rotational motion for evaluating changes of protein oligomeric state in solution". In: *European Biophysics Journal* 51.3 (Apr. 2022), pp. 193–204. DOI: 10.1007/s00249-022-01598-w. URL: https://doi.org/10.1007/s00249-022-01598-w.
- [23] Lothar Helm. "Optimization of Gadolinium-Based Mri Contrast Agents for High Magnetic-Field Applications". In: *Future Medicinal Chemistry* 2.3 (Mar. 2010), pp. 385–396. DOI: 10.4155/fmc. 09.174. URL: https://doi.org/10.4155/fmc.09.174.
- [24] Quoc Lam Vuong et al. "Magnetic resonance relaxation induced by superparamagnetic particles used as contrast agents in magnetic resonance imaging: a theoretical review". In: *Wiley Interdisciplinary Reviews Nanomedicine and Nanobiotechnology* 9.6 (Apr. 2017). DOI: 10.1002/wnan. 1468. URL: https://doi.org/10.1002/wnan.1468.
- [25] Mike Jeon et al. "Iron Oxide Nanoparticles as T1 Contrast Agents for Magnetic Resonance Imaging: Fundamentals, Challenges, Applications, and Prospectives". In: *Advanced Materials* 33.23 (June 2020). DOI: 10.1002/adma.201906539. URL: https://doi.org/10.1002/adma.201906539.
- [26] Shahid Ali et al. "Shape- and size-controlled superparamagnetic iron oxide nanoparticles using various reducing agents and their relaxometric properties by Xigo acorn area". In: *Applied Nanoscience* 9.4 (Nov. 2018), pp. 479–489. DOI: 10.1007/s13204-018-0907-5. URL: https://doi.org/10.1007/s13204-018-0907-5.
- [27] Raquel G. D. Andrade, Sérgio R. S. Veloso, and Elisabete M. S. Castanheira. "Shape Anisotropic Iron Oxide-Based Magnetic Nanoparticles: Synthesis and Biomedical Applications". In: *International Journal of Molecular Sciences* 21.7 (Apr. 2020), p. 2455. DOI: 10.3390/ijms21072455. URL: https://doi.org/10.3390/ijms21072455.
- [28] A. Van Oosterom and T.F. Oostendorp. *Medische fysica*. Nov. 2015. DOI: 10.1007/978-90-368-1086-9. URL: https://doi.org/10.1007/978-90-368-1086-9.
- [29] Sophie L. Nedelec et al. "Particle motion: the missing link in underwater acoustic ecology". In: Methods in Ecology and Evolution 7.7 (Feb. 2016), pp. 836–842. DOI: 10.1111/2041-210x.12544. URL: https://doi.org/10.1111/2041-210x.12544.
- [30] Valeria Garbin et al. "Unbinding of targeted ultrasound contrast agent microbubbles by secondary acoustic forces". In: *Physics in Medicine and Biology* 56.19 (Aug. 2011), pp. 6161–6177. DOI: 10.1088/0031-9155/56/19/002. URL: https://doi.org/10.1088/0031-9155/56/19/002.
- [31] Pierre-Yves Gires et al. "The acoustic radiation force: a gravitation-like field". In: arXiv (Cornell University) (Jan. 2018). DOI: 10.48550/arxiv.1805.01634. URL: https://arxiv.org/abs/1805.01634.
- [32] L O Bowen. "Nuclear magnetic acoustic resonance in non-viscous liquids". In: *British Journal of Applied Physics* 15.11 (Nov. 1964), pp. 1451–1452. DOI: 10.1088/0508-3443/15/11/136. URL: https://doi.org/10.1088/0508-3443/15/11/136.

[33] Pijush K. Kundu, Ira M. Cohen, and David R. Dowling. *Vorticity Dynamics*. July 2015, pp. 195–226. DOI: 10.1016/b978-0-12-405935-1.00005-8. URL: https://doi.org/10.1016/b978-0-12-405935-1.00005-8.

- [34] O.M. Amoo and A. Falana. *Numerical techniques for the solution of the laminar boundary layer equations*. Jan. 2020, pp. 233–258. DOI: 10.1016/b978-0-12-817949-9.00018-9. URL: https://doi.org/10.1016/b978-0-12-817949-9.00018-9.
- [35] Seongho Jeon et al. "Quantifying intra- and extracellular aggregation of iron oxide nanoparticles and its influence on specific absorption rate". In: *Nanoscale* 8.35 (Jan. 2016), pp. 16053–16064. DOI: 10.1039/c6nr04042j. URL: https://doi.org/10.1039/c6nr04042j.
- [36] James Corson, George W. Mulholland, and Michael R. Zachariah. "Analytical expression for the rotational friction coefficient of DLCA aggregates over the entire Knudsen regime". In: *Aerosol Science and Technology* 52.2 (Oct. 2017), pp. 209–221. DOI: 10.1080/02786826.2017.1390544. URL: https://doi.org/10.1080/02786826.2017.1390544.
- [37] Oleksandr Tomchuk. "Models for Simulation of Fractal-like Particle Clusters with Prescribed Fractal Dimension". In: *Fractal and Fractional* 7.12 (Dec. 2023), p. 866. DOI: 10.3390/fractalfract7120866. URL: https://doi.org/10.3390/fractalfract7120866.
- [38] D Eberbeck et al. "Aggregation behaviour of magnetic nanoparticle suspensions investigated by magnetorelaxometry". In: *Journal of Physics Condensed Matter* 18.38 (Sept. 2006), S2829—S2846. DOI: 10.1088/0953-8984/18/38/s20. URL: https://doi.org/10.1088/0953-8984/18/38/s20.
- [39] Chonglin Zhang et al. "Determination of the Scalar Friction Factor for Nonspherical Particles and Aggregates Across the Entire Knudsen Number Range by Direct Simulation Monte Carlo (DSMC)". In: *Aerosol Science and Technology* 46.10 (May 2012), pp. 1065–1078. DOI: 10.1080/02786826.2012.690543. URL: https://doi.org/10.1080/02786826.2012.690543.
- [40] Bradley E. Treeby and B. T. Cox. "k-Wave: MATLAB toolbox for the simulation and reconstruction of photoacoustic wave fields". In: *Journal of Biomedical Optics* 15.2 (2010), p. 021314. DOI: 10.1117/1.3360308. URL: https://doi.org/10.1117%2F1.3360308.
- [41] Kira Seleznyova, Mark Strugatsky, and Janis Kliava. "Modelling the magnetic dipole". In: *European Journal of Physics* 37.2 (Feb. 2016), p. 025203. DOI: 10.1088/0143-0807/37/2/025203. URL: https://doi.org/10.1088/0143-0807/37/2/025203.
- [42] Yansong Gu et al. "NMR Longitudinal Relaxation Time for Characterizing Oil Occurrence in Shale Organic Nanopores: Insights from the Molecular Level". In: *Colloids and Surfaces A Physicochemical and Engineering Aspects* (Dec. 2024), p. 136048. DOI: 10.1016/j.colsurfa.2024.136048. URL: https://doi.org/10.1016/j.colsurfa.2024.136048.
- [43] L. P. Gor'kov. "On the forces acting on a small particle in an acoustical field in an ideal fluid". In: Soviet physics. Doklady 6 (Jan. 1962), pp. 773–775. URL: https://ci.nii.ac.jp/naid/20000152384/.
- [44] Henrik Bruus. "Acoustofluidics 10: Scaling laws in acoustophoresis". In: *Lab on a Chip* 12.9 (Jan. 2012), p. 1578. DOI: 10.1039/c2lc21261g. URL: https://doi.org/10.1039/c2lc21261g.
- [45] Henrik Bruus. "Acoustofluidics 7: The acoustic radiation force on small particles". In: *Lab on a Chip* 12.6 (Jan. 2012), p. 1014. DOI: 10.1039/c2lc21068a. URL: https://doi.org/10.1039/c2lc21068a.
- [46] B. V. Derjaguin. "Theory of the stability of strongly charged lyophobic sols and the adhesion of strongly charged particles in solutions of electrolytes". In: *Acta Physicochim* 14 (Jan. 1941), pp. 633–662. URL: https://ci.nii.ac.jp/naid/10012872964.
- [47] E. J. W. Verwey and J. Th. G Overbeek. *Theory of the stability of lyophobic colloids: the interaction of sol particles having and electric double I layer.* Jan. 1948. URL: http://ci.nii.ac.jp/ncid/BA17705966.
- [48] H. Qian, M.P. Sheetz, and E.L. Elson. "Single particle tracking. Analysis of diffusion and flow in two-dimensional systems". In: *Biophysical Journal* 60.4 (Oct. 1991), pp. 910–921. DOI: 10.1016/s0006-3495(91)82125-7. URL: https://doi.org/10.1016/s0006-3495(91)82125-7.

[49] Diego Krapf et al. "Power spectral density of a single Brownian trajectory: what one can and cannot learn from it". In: *New Journal of Physics* 20.2 (Jan. 2018), p. 023029. DOI: 10.1088/1367-2630/aaa67c. URL: https://doi.org/10.1088/1367-2630/aaa67c.

- [50] Seán Moran. *An Applied Guide to Water and Effluent Treatment Plant Design*. Jan. 2018. DOI: 10.1016/c2016-0-01092-6. URL: https://doi.org/10.1016/c2016-0-01092-6.
- [51] J Theodore et al. "Transalveolar transport of large polar solutes (sucrose, inulin, and dextran)". In: American Journal of Physiology-Legacy Content 229.4 (Oct. 1975), pp. 989–996. DOI: 10.1152/ajplegacy.1975.229.4.989. URL: https://doi.org/10.1152/ajplegacy.1975.229.4.989.
- [52] Thomas Schwarz, Guillaume Petit-Pierre, and Jurg Dual. "Rotation of non-spherical micro-particles by amplitude modulation of superimposed orthogonal ultrasonic modes". In: *The Journal of the Acoustical Society of America* 133.3 (Mar. 2013), pp. 1260–1268. DOI: 10.1121/1.4776209. URL: https://doi.org/10.1121/1.4776209.
- [53] Glauber T. Silva. "Acoustic radiation force and torque on an absorbing compressible particle in an inviscid fluid". In: *The Journal of the Acoustical Society of America* 136.5 (Nov. 2014), pp. 2405–2413. DOI: 10.1121/1.4895691. URL: https://doi.org/10.1121/1.4895691.
- [54] Pierre-Olivier Champagne et al. "Colloidal Stability of Superparamagnetic Iron Oxide Nanoparticles in the Central Nervous System: A Review". In: *Nanomedicine* 13.11 (June 2018), pp. 1385–1400. DOI: 10.2217/nnm-2018-0021. URL: https://doi.org/10.2217/nnm-2018-0021.
- [55] Vin Cent Tai et al. "Decoding iron oxide nanoparticles from design and development to real world application in water remediation". In: *Journal of Industrial and Engineering Chemistry* 127 (July 2023), pp. 82–100. DOI: 10.1016/j.jiec.2023.07.038. URL: https://doi.org/10.1016/j.jiec.2023.07.038.
- [56] Antony V. Samrot et al. "A review on synthesis, characterization and potential biological applications of superparamagnetic iron oxide nanoparticles". In: Current Research in Green and Sustainable Chemistry 4 (Dec. 2020), p. 100042. DOI: 10.1016/j.crgsc.2020.100042. URL: https://doi.org/10.1016/j.crgsc.2020.100042.
- [57] Carlotta Pucci et al. "Superparamagnetic iron oxide nanoparticles for magnetic hyperthermia: recent advancements, molecular effects, and future directions in the omics era". In: *Biomaterials Science* 10.9 (Jan. 2022), pp. 2103–2121. DOI: 10.1039/d1bm01963e. URL: https://doi.org/10.1039/d1bm01963e.
- [58] Wen Zhang et al. "Attachment Efficiency of Nanoparticle Aggregation in Aqueous Dispersions: Modeling and Experimental Validation". In: *Environmental Science & Technology* 46.13 (Jan. 2012), pp. 7054–7062. DOI: 10.1021/es203623z. URL: https://doi.org/10.1021/es203623z.
- [59] Vital Cruvinel Ferreira-Filho et al. "Influence of SPION Surface Coating on Magnetic Properties and Theranostic Profile". In: *Molecules* 29.8 (Apr. 2024), p. 1824. DOI: 10.3390/molecules290 81824. URL: https://doi.org/10.3390/molecules29081824.
- [60] Somayeh Mirsadeghi et al. "Effect of PEGylated superparamagnetic iron oxide nanoparticles (SPIONs) under magnetic field on amyloid beta fibrillation process". In: *Materials Science and Engineering C* 59 (Oct. 2015), pp. 390–397. DOI: 10.1016/j.msec.2015.10.026. URL: https://doi.org/10.1016/j.msec.2015.10.026.
- [61] Bertrand Faure, German Salazar-Alvarez, and Lennart Bergström. "Hamaker Constants of Iron Oxide Nanoparticles". In: *Langmuir* 27.14 (June 2011), pp. 8659–8664. DOI: 10.1021/la201387d. URL: https://doi.org/10.1021/la201387d.
- [62] Pratima Bajpai. *Hydraulics*. Jan. 2018, pp. 455–482. DOI: 10.1016/b978-0-12-814238-7. 00023-4. URL: https://doi.org/10.1016/b978-0-12-814238-7.00023-4.
- [63] Vibha Kalra, Fernando Escobedo, and Yong Lak Joo. "Effect of shear on nanoparticle dispersion in polymer melts: A coarse-grained molecular dynamics study". In: *The Journal of Chemical Physics* 132.2 (Jan. 2010). DOI: 10.1063/1.3277671. URL: https://doi.org/10.1063/1.3277671.

[64] Bowen Lv et al. "Development of a comprehensive understanding of aggregation-settling movement of CeO2 nanoparticles in natural waters". In: *Environmental Pollution* 257 (Nov. 2019), p. 113584. DOI: 10.1016/j.envpol.2019.113584. URL: https://doi.org/10.1016/j.envpol.2019.113584.

- [65] Bashiru Kayode Sodipo and Azlan Abdul Aziz. "Effect of sonication on the colloidal stability of iron oxide nanoparticles". In: *AIP conference proceedings* (Jan. 2015). DOI: 10.1063/1.4915167. URL: https://doi.org/10.1063/1.4915167.
- [66] Van Son Nguyen et al. "Effect of ultrasonication and dispersion stability on the cluster size of alumina nanoscale particles in aqueous solutions". In: *Ultrasonics Sonochemistry* 18.1 (July 2010), pp. 382–388. DOI: 10.1016/j.ultsonch.2010.07.003. URL: https://doi.org/10.1016/j.ultsonch.2010.07.003.
- [67] Sophie Laurent et al. "ChemInform Abstract: Magnetic Iron Oxide Nanoparticles: Synthesis, Stabilization, Vectorization, Physicochemical Characterizations, and Biological Applications". In: *ChemInform* 39.35 (Aug. 2008). DOI: 10.1002/chin.200835229. URL: https://doi.org/10.1002/chin.200835229.
- [68] Mohammed Baalousha et al. "Aggregation and surface properties of iron oxide nanoparticles: Influence of ph and natural organic matter". In: *Environmental Toxicology and Chemistry* 27.9 (Apr. 2008), pp. 1875–1882. DOI: 10.1897/07-559.1. URL: https://doi.org/10.1897/07-559.1.



Acoustic radiation force in standing wave

In applications such as acoustophoresis, which refers to the movement of particles due to acoustic pressure [44], the net movement of the particle is determined by the acoustic radiation force (F^{rad}), which represents the time-averaged instantaneous force. The equation for the acoustic radiation forces on compressible particles with radii much smaller than the wavelength has been derived by Gor'kov [43] and is defined as the gradient of the acoustic potential, also referred to as the Gor'kov potential (U^{rad}) as follows:

$$F^{rad} = -\nabla U^{rad} \tag{A.1}$$

For a two-dimensional case of a compressible spherical particle suspended in an infinite inviscid fluid, exposed to an acoustical pressure field of a standing wave, the acoustic potential is given by [43, 45, 52]:

$$U^{rad} = \frac{4\pi}{3}r^3 \left[\frac{f_1 \kappa_0}{2} \langle p_{in}^2 \rangle - \frac{3f_2 \rho_0}{4} \langle v_{in}^2 \rangle \right] \tag{A.2}$$

where $\langle p_{in} \rangle$ and $\langle v_{in} \rangle$ are the time-averaged pressure and velocity, which have been averaged over one period of the sound wave. f_1 and f_2 refer to the monopole and dipole scattering coefficients, respectively, with $f_1=1-\frac{\kappa_s}{\kappa_0}$ and $f_2=\frac{2(\rho_s-\rho_0)}{(2\rho_s+\rho_0)}$. κ_0 and ρ_0 refer to the compressibility and density of the suspension, and κ_s and ρ_s refer to the compressibility and density of the SPIONs. For SPIONs, $f_1\approx 1$ and $f_2\approx \frac{1}{2}$. Based on this relationship, the equation for the acoustic radiation force in the x direction is written as follows:

$$F_x^{rad} = \pi r^3 P_a^2 \kappa_0 k \left[\frac{1}{3} f_1 + \frac{1}{2} f_2 \right] \sin(2k_0 x)$$
 (A.3)

where P_a denotes the time-invariant pressure and k the wavenumber. For a progressive plane wave, the acoustic radiation force is given by [53]:

$$F_x^{rad} = \pi r^2 (kr)^4 \frac{4P_a^2 \kappa_0}{18} \left[f_1^2 + f_1 f_2 + \frac{3f_2^2}{4} \right]$$
 (A.4)

Equation A.3 and A.4 highlight the fact that the acoustic radiation force is a time-averaged quantity that depends only on the spatial characteristics of the acoustic field. This means that it describes the net force experienced by a particle, resulting in a net motion over time. It does not describe any

instantaneous force on the particle, meaning that oscillatory dynamics of the particle at the frequency of the sound wave (and thus the Larmor frequency) are left out. This highlights the essence of an instantaneous acoustic force description such that the dynamics of the particle at the Larmor frequency can be determined.



Determining factors for SPION aggregation

SPION clusters form when the factors that promote aggregation outweigh the factors that oppose aggregation [54]. The process of aggregation can be divided in two steps, 'collision' and 'adhesion'. Here, collision refers to the process of the nanoparticles moving through the fluid and colliding. Adhesion refers to the formation of clusters as a result of forces between the SPIONs [55]. Among a large number of mechanisms, the most important factors determining the formation of SPION clusters are Brownian motion, hydrodynamic flow and SPION concentration [56]. The next part highlights the determining factors for the formation of SPION clusters, which are summarized in Table B.1.

Process	Mechanism	Pro / Anti	
	Magnetic force	Pro-aggregation	
Adhesion	Van der Waals forces	Pro-aggregation	
	Coating (steric/electrostatic)	Anti-aggregation	
	Age	Pro-aggregation	
	Brownian motion	Both	
Collision	SPION concentration	Pro-aggregation	
Comsion	Acoustic streaming	Anti-aggregation	

Table B.1: Factors influencing SPION aggregation.

B.1. Brownian motion

Brownian motion cannot be classified as either pro- or anti-aggregation because it can promote both of these. Brownian motion causes the random movement of particles, resulting in a higher probability of collisions, and thus a higher probability of the formation of SPION clusters. On the other hand, the kinetic energy due to Brownian motion can lead to destruction of weakly formed molecular bonds [54]. Brownian motion in SPIONs is dependent on size, the temperature of the solvent and viscosity, as shown in Equation B.1.

$$\tau_B = \frac{3\eta V_H}{k_B T} \tag{B.1}$$

Here, τ_B is the Brownian relaxation time, which represents the characteristic time it takes for a nanoparticle and its magnetic moment to return to equilibrium after being disturbed, causing friction with the medium [57]. η , V_H , k_B and T represent the viscosity of the medium, the hydrodynamic volume of the nanoparticle, the Boltzmann constant, and the ambient temperature, respectively.

SPIONs in a highly viscous medium will experience significant drag, which decreases the Brownian motion. This relationship is described in the Stokes–Einstein–Debye relation, where the rotational drag coefficient (ζ_r) of a spherical particle is given by $\zeta=8\pi\eta r^3$, r being the radius of the SPIONs [36]. The same effect can be seen in Equation B.1, where τ_B increases linearly as η increases, indicating that it takes the nanoparticle longer to return to equilibrium.

The temperature of the medium influences the Brownian motion as well, with larger temperatures increasing the Brownian motion. The ambient temperature will therefore also affect aggregation of SPI-ONs.

Lastly, nanoparticle size is of great influence on Brownian motion. As the radius of the particle increases, τ_B increases to the third power, which can induce both aggregation and disaggregation. However, in a study by W. Zhang et al., where an attempt was made to model nanoparticle aggregation, it was shown that smaller particles tend to aggregate more than larger ones [58]. Another study by Ferreira-Filho et al., where SPIONs were coated with both dextran and gold, supported this same effect and showed that larger particles have a lower tendency to aggregate [59]. Furthermore, it is well understood that SPION coating will affect their electrostatic and steric behaviour (as discussed in section B.3) [54]. This has also been investigated by Mirsadeghi et al., where it was shown that SPIONs coated with Polyethylene Glycol (PEG), PEG-NH₂ or PEG-COOH exhibit different hydrodynamic volumes due to varying surface charges [60]. This in turn results in different values for τ_B .

B.2. Pro-aggregation factors

As mentioned, the superparamagnetic characteristic of SPIONs causes the nanoparticle to have no residual magnetization in the absence of a magnetic field. Furthermore, due to both Brownian motion and intrinsic flipping of the dipoles of the SPION, the net magnetization of all SPIONs is zero. However, when the magnetic field is turned on, the SPIONs reach saturation magnetization and the dipoles align due to the magnetic force [54]. As a result, the SPIONs will aggregate and lose the superparamagnetism property.

Another pro-aggregation force are van der Waals forces. This attractive force decreases with increasing distance between similar particles [54]. The magnitude of the force is also determined by the radius of the particle and the Hamaker constant, which is a parameter that depends on the dielectric properties of the nanoparticles and solvent [61]. Both the magnetic force and van der Waals force facilitate adhesion.

A factor that can facilitate collisions is the concentration of SPIONs. This can simply be explained by the fact that a higher concentration of SPIONs increases the probability of collisions, which can increase clustering [60]. Interestingly, in a study by Eberbeck et al. that attempts to model the fraction of SPION aggregates in a fluid, it was found that the fraction of large aggregates decreased upon dilution of the sample [38]. The authors suggest that this behaviour is influenced by the age of the solution. The authors note that over time the colloidal stability of the surface of the SPION decreases, indicating that aging can also be a determinant factor for the aggregation of SPIONs.

B.3. Anti-aggregation factors

An effect that decreases aggregation, is hydrodynamic flow, which refers to the fluids in motion [62]. Research has shown conflicting results on the effect of hydrodynamic flow on collision frequency of nanoparticles. For instance, Kalra et al. showed that the SPIONs will experience a force which is tangential to the surface, promoting particle dispersion and a decrease in frequency collisions [63]. On the other hand, Lv et al. demonstrated that the shear force in the fluid increases the collision frequency by 4 to 5 orders of magnitude, theoretically promoting aggregation [64]. However, Lv et al. also observed that despite the increased collision frequency, the dominant effect of hydrodynamic flow appears to be disaggregation, driven by other mechanisms. This suggests that while hydrodynamic flow can lead to more particle collisions, its overall net effect is disaggregation.

In the case of resonant US waves in NMR, the hydrodynamic flow is mainly a result of the acoustic radiation pressure applied to the sample. The hydrodynamic flow induced by the US wave is called acoustic streaming. As acoustic streaming creates shear forces in the medium, it is expected that

aggregation of SPIONs will be hindered. However, research has shown that the zeta potential (ζ) of SPIONs, which indicates the electric potential between the diffuse layer and the solution, is drastically reduced above a pH of 4 when exposed to an US wave, thus decreasing the colloidal stability and increasing the probability of aggregation [65]. Interestingly, this effect is in conflict with the established understanding of acoustic streaming, which is known for its ability to form, grow and implode bubbles in the sample, leading to disaggregation of nanoparticles in general [66]. As research on the effect of acoustic streaming on the behaviour of SPIONs is limited, the exact influence is uncertain.

Coating plays a considerable role in the colloidal stability of the SPIONs, but many studies have also shown the influence of coating on the magnetic properties [15, 59, 60]. However, the main function of the coating is to prevent adhesion of the SPIONs, while keeping magnetic properties similar. In the case of magnetic nanoparticles in a suspension, there are four forces that contribute to the potential between particles. Thus far, van der Waals and magnetic forces have been discussed as attractive forces causing aggregation. The remaining two forces are steric and electrostatic forces and act as repulsive forces [67]. A theory used to describe the stability of nanoparticles in suspension is the Derjaguin–Landau–Verwey–Overbeek (DLVO) theory that considers the van der Waals force and the electrostatic force [46, 47].

Electrostatic forces, illustrated in Figure B.1, are the repulsive forces between charged particles as a result of the ionic concentration and the pH of the solution [67]. Electrostatic forces are often quantified by the ζ -potential, where large positive or negative values for ζ indicate a strong repulsion. The closer ζ is to zero, the lower the repulsion and the more likely the SPIONs are to aggregate. The higher the ionic concentration or pH, the lower these repulsive forces become, resulting in an increased probability of cluster formation. This mechanism was demonstrated by Jeon et al. where high salt concentrations were used to promote SPION clustering containing 10^3 [35]. Furthermore, Baalousha et al. illustrated that aggregation of SPIONs in a water solution increased at higher pH and reached a maximum at a pH of 8.5 [68].

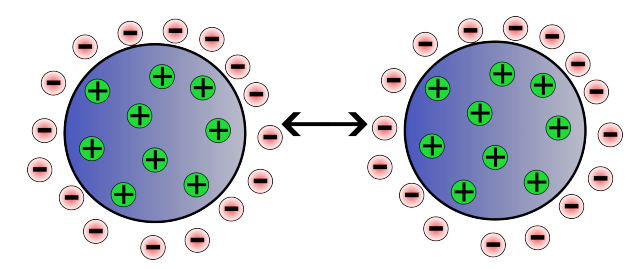


Figure B.1: Electrostatic repulsion of positively charged SPIONs.

Steric forces, as depicted in Figure B.2, are a result of the overlap of coatings consisting of long-chain molecules. When two particles approach each other, this overlap leads to an increase in entropy, preventing adhesion [54]. Changing the coating could therefore drastically increase the steric force between particles. One of the most used coatings are dextran and polyethylene glycol (PEG). Both coatings ensure steric forces large enough to promote colloidal stability [54].

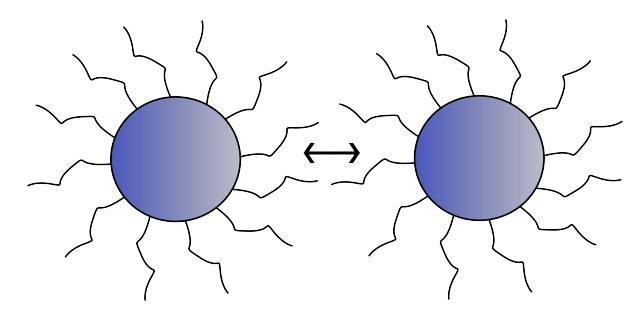


Figure B.2: Steric repulsion of coated SPIONs.



Preparatory T_1 and T_2 NMR measurements

 T_1 and T_2 measurements on the SPION solutions from Table 3.2 were performed using an SR sequence and a CPMG sequence, respectively. The samples were diluted logarithmically following Equation C.1.

$$C_n = C_0 \cdot \left(\frac{1}{2}\right)^n \tag{C.1}$$

In this equation, C_n denotes the concentration of the n^{th} dilution step, C_0 is the initial (stock) concentration of the SPION solution as listed in Table 3.2, and n represents the dilution step number, where each step corresponds to a 1:2 dilution.

Per dilution, 10 measurements on T_1 and T_2 were conducted for varying values of n until longitudinal relaxation rates of approximately 10^0 were measured. The relaxation rates were then averaged over the number of measurements, and standard deviations were calculated. To indicate the goodness of the fit to the data, the coefficient of determination R^2 was determined. Fits with $R^2 < 0.8$ were deemed insufficiently reliable and were excluded from the calculation of average T_1 and T_2 values. Additionally, for synomag®-D (50 nm), very short relaxation times combined with suboptimal NMR measurement settings limited the measurable range to T_1 values at concentrations of 0.625 mg/ml and lower, and T_2 values at 5 mg/ml and lower. The results for the relaxation rates (1/s) as a function of the SPION concentration in mg/ml are shown in Figure C.1.

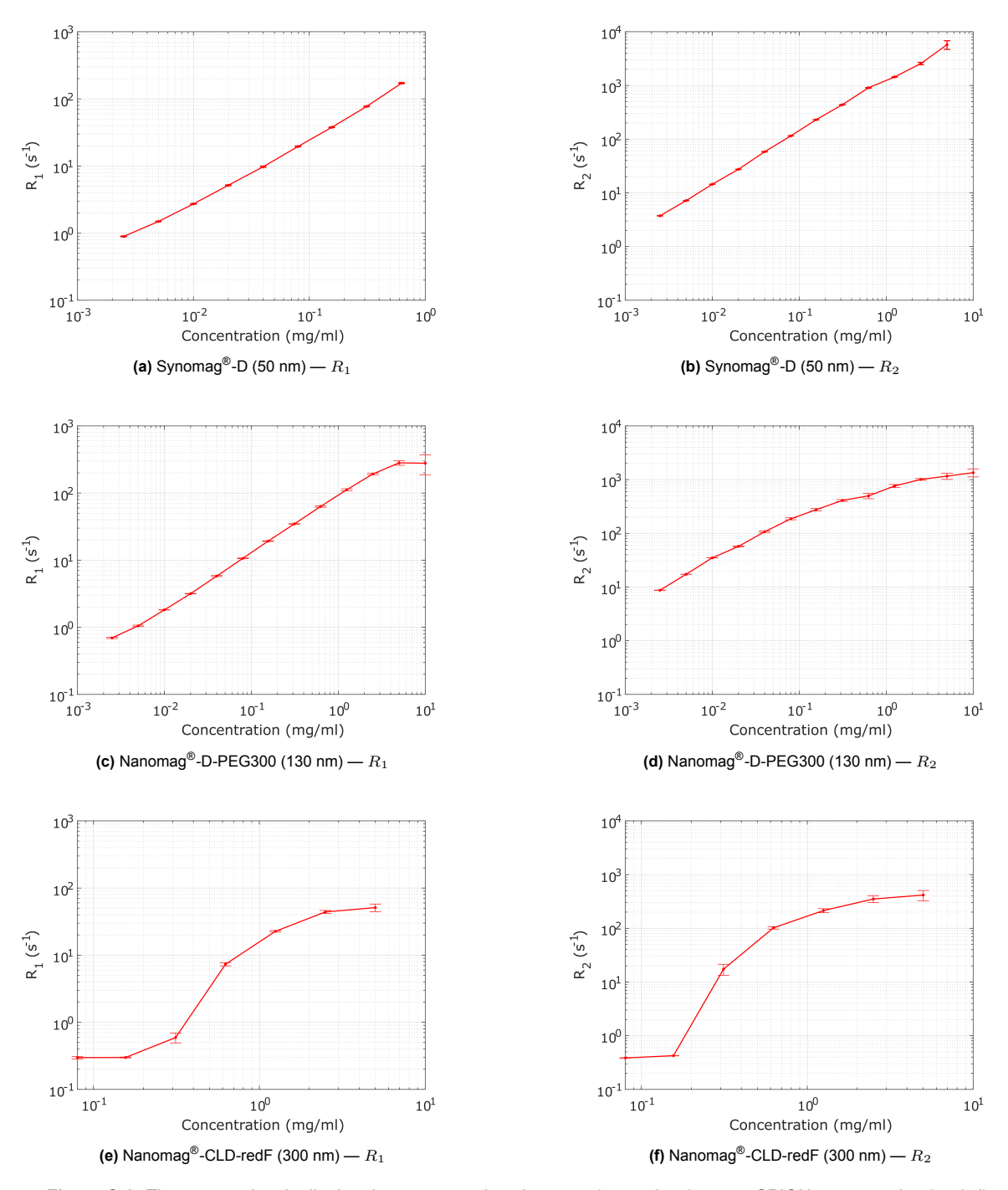


Figure C.1: The average longitudinal and transverse relaxation rates $(R_1 \text{ and } R_2)$ versus SPION concentration (mg/ml) including standard deviation for the SPION solutions described in Table 3.2.



T_1 and T_2 NMR measurements over time

To visualize the drift in T_1 and T_2 over time for the SPION solutions, a short measurement of around 1500 seconds on the relaxation times was performed. These measurements were performed on the nanomag®-D-PEG300 with a concentration of 0.03 mg/ml. The results are shown in Figure D.1. An increase in both relaxation times can be observed.

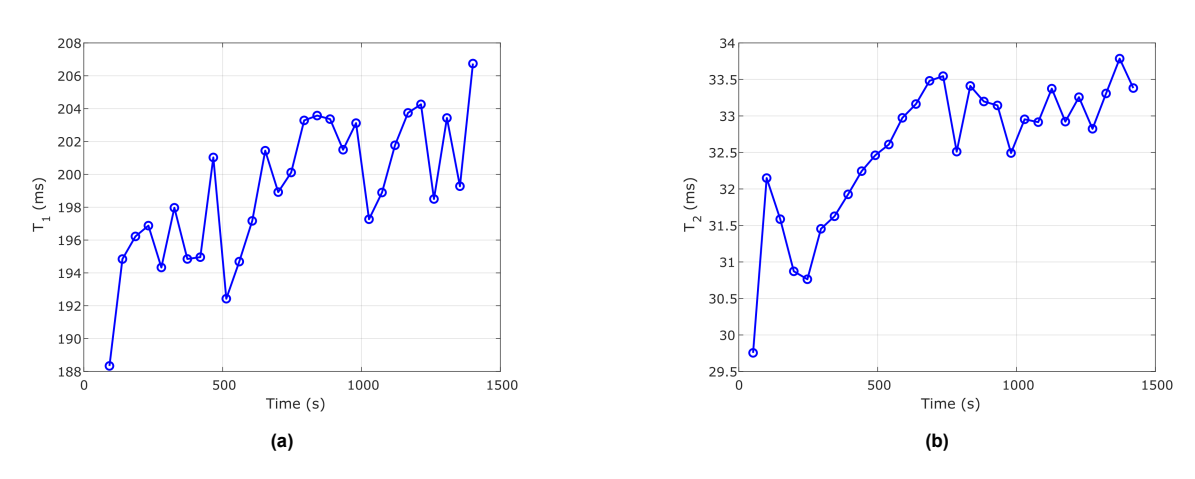


Figure D.1: The measured longitudinal (a) and transverse (b) relaxation times for nanomag[®]-D-PEG300 with a concentration of 0.03 mg/ml. An increase in relaxation times over time can be observed.